This is a preprint, the final version is subject to change, of the American Mineralogist (MSA)
Cite as Authors (Year) Title. American Mineralogist, in press.
DOI: https://doi.org/10.2138/am-2020-7189

Revision 2

Thermoelasticity of Tremolite Amphibole: Geophysical Implications

Ye Peng[1], Mainak Mookherjee

Earth Materials Laboratory, Department of Earth, Ocean and Atmospheric Science,

Florida State University, Tallahassee, FL 32306, USA

[1]*corresponding author*: yp16b@my.fsu.edu

Abstract

We investigated the structure, equation of state, thermodynamic, and elastic properties of tremolite amphibole ($Ca_2Mg_5Si_8O_{22}(OH)_2$) up to 10 GPa and 2000 K, using *first principles* simulations based on density functional perturbation theory. We found that at 300 K, the pressure-volume results can be adequately described by a third-order Birch-Murnaghan equation of state with bulk moduli K_0 of 78.5 and 66.3 GPa based on local density approximation (LDA) and generalized gradient approximation (GGA), respectively. We also derived its coefficients of the elastic tensor based on LDA and GGA and found that the LDA is in good agreement with the experimental results. At 300 K, the shear modulus G_0 is 58.0 GPa based on LDA. The pressure derivative of the bulk modulus K' is 5.9 while that of the shear modulus G' is 1.3. The second Grüneisen parameter, or $\delta_T = [-1/(\alpha K_T)](\partial K_T/\partial T)_P$, is 3.3 based on LDA. We found that at ambient conditions, tremolite is elastically anisotropic with the compressional wave velocity anisotropy AV_P being 34.6% and the shear wave velocity anisotropy AV_S being 27.5%. At higher pressure corresponding to the thermodynamic stability of tremolite, i.e., ~3 GPa, the AV_P reduces to 29.5% whereas AV_S increases to 30.8%. To evaluate whether the presence of hydrous phases such as amphibole and phlogopite could account for the observed shear wave velocity (V_S) anomaly at the mid-lithospheric discontinuity (MLD), we used the thermoelasticities of tremolite (as a proxy for other

amphiboles), phlogopite, and major mantle minerals to construct synthetic velocity profiles. We noted that at depths corresponding to the mid-lithosphere, the presence of 25 vol% amphibole and 1 vol% phlogopite could account for a V_S reduction of 2.3%. Thus based on our thermoelasticity results on tremolite amphibole, it seems that mantle metasomatism could partly explain the MLD.

Keywords: Tremolite, equation of state, elasticity, Mid-Lithospheric Discontinuity (MLD)

Introduction

It is well known that the Earth's surface is made up of rigid plates composed of the crust and the brittle part of the upper mantle, together known as the lithosphere. The lithosphere glides over the rheologically weaker part of the mantle known as the asthenosphere. The lithosphere and asthenosphere boundary (LAB) is characterized by a negative seismic shear wave velocity gradient (dV_S/dz; where V_S refers to the seismic shear wave velocity and z refers to the depth from the surface). This reduction of V_S is thought to indicate the presence of partial melts at the LAB, as the conductive geothermal gradient of the relatively colder lithosphere intersects the solidus of mantle lithologies (Rychert et al., 2005; Rychert and Shearer, 2009; Fischer et al., 2010).

Recent high resolution, short-wavelength body wave studies across continents revealed a 3-10% reduction in V_S at depths ranging between 50 and 160 km. This drop in V_S is a nearly global phenomenon (Abt et al., 2010; Selway et al., 2015). In most regions where velocity drops have been reported, the depth range is tightly confined between 80-100 km, which is in the middle of the continental lithosphere. Therefore, this V_S anomaly is referred to as the mid-lithospheric discontinuity (MLD) (Abt et al., 2010; Fischer et al., 2010). This is distinct from the LAB, which often occurs at depths between 150 and 300 km beneath the surface of the

continental crust and is associated with a smaller velocity reduction than that of the MLD in many regions (Karato et al., 2015). The velocity anomaly at the MLD is a rather perplexing observation and challenges the existing view that the geologically older cratons (age > 540 Ma) in the inner part of the continents are tectonically stable. The current understanding that the craton is stable over long geological time is based on geochemical studies of upper mantle rocks (Carlson et al., 2005) and long wavelength surface wave studies (Gung et al., 2003). The key question is what could cause such a reduction of velocity at MLD depths. The reduction in V_S could be related to the presence of partial melts (Fischer et al., 2010) such that they are interconnected across the matrix of the host rock. This is likely to affect the strength of the bulk rock and then the longevity of the craton as mechanically strong layers. However, the continental geotherm at MLD depths is unlikely to be hot enough to generate partial melts (Karato et al., 2015). Alternative mechanisms have also been proposed to explain the V_S reduction and include anisotropy (Yuan and Romanowicz, 2019; Selway et al., 2015), elastically accommodated grain boundary sliding (EAGBS) (Karato et al., 2015; Karato and Park, 2019), and mantle metasomatism (Selway et al., 2015; Saha et al., 2018). Both azimuthal and radial anisotropy could produce MLD features. Yet, the azimuthal anisotropy is dependent on the station-source configurations, i.e., back-azimuths. The geometries of radial anisotropy are only observed locally and are hard to explain tectonically (Selway et al., 2015). A rheological change as in EAGBS is an elegant mechanism that could explain the lowering of V_S. The velocity reduction caused by EAGBS when it occurs solely due to temperature is not sharp enough to be detectable, even by the short-wavelength body wave studies (Selway et al., 2105; Karato et al., 2015). The presence of a water-rich or compositionally different layer is likely to further enhance the velocity reduction (Karato et al., 2015). However, the effect of water on the seismic wave velocity and attenuation is quite complex and certainly warrants further study (Cline II et al., 2018; Mittal et al., 2019).

Mantle metasomatism is likely to stabilize hydrous phases including amphiboles and micas (Selway et al., 2015; Saha et al., 2008), which have substantially lower seismic velocities than major mantle minerals (Abers and Hacker, 2016). Therefore, these hydrous phases might create the velocity drops necessary to explain the MLD.

Amphiboles are likely to be stable over a wide range of pressures (<3-4 GPa), temperatures (<1100 °C), and chemistries pertaining to the metasomatized mantle (Mandler and Grove, 2016). The P-T limit of the thermodynamic stability of amphiboles is nearly flat i.e., $dP/dT \approx 0$ (Mandler and Grove, 2016; Frost, 2006). This indicates that the high pressure stability of amphiboles is not sensitive to temperature. Thus, upon mantle metasomatism, amphiboles are likely to be stabilized at pressures of ~3-4 GPa, corresponding to depths of ~90-120 km across a wide variety of geotherms. The calcic end member, tremolite, is stable up to ~3 GPa and has a similar dP/dT trend, and hence it could be used as a proxy for other amphibole phases that are likely to be stable in the metasomatized mantle (Jenkins et al., 1991).

Although amphiboles are common rock-forming minerals in both the crust and the upper mantle across diverse geological settings, our understanding of their thermoelastic properties at relevant pressures and temperatures conditions remains poor. Thus, having a better constraint on those of amphiboles is critical to better understand the geological processes that might explain the MLD. The crystal structure of amphibole accommodates a wide variety of cations and it forms an extensive solid solution with many end member stoichiometries. Over the broad range of amphibole end member compositions (e.g., tremolite, pargasite, glaucophane, kaesurite), the most commonly reported elastic properties are from equation of state studies using powder or single-crystal X-ray diffraction (XRD) (Comodi et al., 1991; Zhang et al., 1992; Yang et al., 1998; Comodi et al., 2010; Jenkins et al., 2010; Zanazzi et al., 2010; Welch et al., 2011; Nestola et al., 2012). More recently, the thermal

equation of state of the end member pargasite has been experimentally determined (Comboni et al., 2017). These available experimental studies on the thermoelastic properties of amphiboles provide constraints only on the bulk moduli and their pressure/temperature derivatives. However, to relate to the geophysical observations, one also requires a better constraint on the shear moduli, which are not determined from the equation of state studies. Moreover, the bulk moduli reported from the single-crystal equation of state are often the Reuss bound which are significantly smaller than the Voigt-Reuss-Hill or Hashin-Shtrikman averages used for estimating the seismic velocities in absence of crystal preferred orientations (Brown and Abramson, 2016). For instance, the existing thermoelastic database (Abers and Hacker, 2016) tabulates bulk moduli of tremolite and pargasite determined from the single-crystal XRD study (Comodi et al., 1991), i.e., the bulk moduli are likely to be underestimated. In a recent experimental study, the coefficients of the elastic tensor of calcic and sodic-calcic amphiboles at ambient conditions were reported using impulsive stimulated light scattering method (Brown and Abramson, 2016). However, the effects of pressure and temperature on the elasticity of amphiboles remain largely unknown.

To provide better constraints on the elasticity of amphibole at high pressures and temperatures relevant for the MLD, in this study we report the elastic properties of tremolite ($Ca_2Mg_5Si_8O_{22}(OH)_2$) using *first principles* simulations based on the static Density Functional Theory (DFT). We explore the structure and elasticity of tremolite up to a pressure of 10 GPa, beyond its thermodynamic stability. We also explore the effect of temperature on the coefficients of the elastic tensor by including thermal corrections to the static pressures based on quasi-harmonic approximations (QHA). We combine the thermoelastic properties of tremolite as a proxy for amphiboles with those of the major mantle minerals to construct the lithospheric mantle velocity-depth profiles and relate them to geophysical observations.

126

127 **Methods**

128 Tremolite is a calcic amphibole with a stoichiometry of $Ca_2Mg_5Si_8O_{22}(OH)_2$. In order
129 to compute elastic properties of tremolite, we used the crystal structure of natural near-end-
130 member tremolite determined by single-crystal XRD (Yang and Evans, 1996) as a starting
131 guess and modified it to match the pure end-member composition. The unit cell of tremolite
132 consists of 82 atoms, i.e., two formula units (Z= 2). Tremolite is monoclinic and has a space
133 group symmetry *C*2/*m*. The crystal structure consists of two principal elements: a double
134 chain of corner-sharing tetrahedral units and a strip of edge-sharing octahedral units, both of
135 which extend along the [001] direction. In the double chain, there are two distinct tetrahedral
136 sites, T1 and T2, both occupied by silicon atoms. In the octahedral strip, there are three
137 distinct octahedral sites denoted by M1, M2, and M3, which are occupied by magnesium
138 atoms. The strip of octahedral units is sandwiched between two tetrahedral double chains
139 with their apices pointing towards each other, together forming an I-beam (**Figure 1**). At the
140 junction of the I-beams is the B site, which hosts the calcium atom in distorted cubic
141 coordination. The alkali (A) site is vacant in tremolite. The hydrogen is bonded to an oxygen
142 atom shared by one M3 and two M1 octahedral units. The hydroxyl vector points towards the
143 center of the ditrigonal ring formed by the tetrahedral units (**Figure 1**).

144 We performed *first principles* simulations based on DFT (Hohenberg and Kohn, 1964;
145 Kohn and Sham, 1965), with a highly accurate plane-wave basis projector augmented wave
146 method as implemented in the Vienna ab initio simulation package (VASP) (Kresse and
147 Hafner, 1993; Kresse and Furthmüller, 1996a, b; Kresse and Joubert, 1999). The method
148 solves the time-independent Schrödinger equation for a multi-electron system. It is widely
149 used for silicate mineral studies such as for mineral structures, energies, and elasticities
150 (Karki et al., 2001; Stixrude et al., 1998). We investigated the mineral properties with two

widely used approximations to the exchange-correlation functional: the local density approximation (LDA) (Ceperley and Adler, 1980) and the generalized gradient approximation (GGA) (Lundqvist and March, 1987; Perdew and Wang, 1986; Perdew et al., 1992). It is known that the ground state energy varies as a function of the plane-wave energy cutoff and the k-point sampling mesh (Peng et al., 2017). We performed a series of convergence tests for tremolite. We found that a plane-wave energy cut-off of 800 eV and a Monkhorst-Pack (Monkhorst and Pack, 1976) k-point mesh of 2x1x4, i.e., 6 irreducible k-points in the Brillouin zone, are sufficient to describe the ground state energies of tremolite. The ground state energies are converged to within 1.3 meV/atom (**Supplementary Table 1**, **2**).

We determined the coefficients of the elastic tensor by a finite difference method (Karki et al., 2001). The coefficients of the elastic tensor (C_{ijkl}) are obtained by relating the stress (σ_{ij}) with the applied strain (ε_{kl}). We applied positive and negative strains of magnitudes 0.5%, 1.0%, 1.5%, and 2.0% to the unit-cell at a specific pressure. The results show a good linear relationship between strains and stresses in the explored strain range (**Supplementary Figure 1**). We found that 1.0% strain is well within the linear elastic limit. This is similar to earlier reports on diverse mineral systems (Karki et al., 2001; Mookherjee and Bezacier, 2012; Peng et al., 2017; Mookherjee et al., 2016, 2019). Hence we applied 1.0% strain for all the investigated volumes. To estimate the effect of the energy cut-off on the convergence of stress, we also computed the coefficients of the elastic tensor at three distinct volumes each with a higher energy cut-off of 1000 eV. We found that the C_{ijkl} with an energy cut-off of 800 eV appears sufficiently converged (**Supplementary Table 3**). We determined the single crystal anisotropy using petrophysical software (Mainprice, 1990).

In order to gain insight into the temperature dependence of the bulk modulus, we performed phonon calculations using density functional perturbation theory (Baroni et al.,

2001) as implemented in VASP (e.g., Gajdoš et al., 2006) and used QHA to estimate the Helmholtz free energy using PHONOPY (Togo and Tanaka, 2015). The Helmholtz free energy under the QHA is given by

$$F(V,T) = U(V) + \frac{1}{2}\sum_{\boldsymbol{q},\nu} \hbar\omega_{\boldsymbol{q},\nu}(V) + k_B T \sum_{\boldsymbol{q},\nu} \ln\left\{1 - \exp\left[\frac{-\hbar\omega_{\boldsymbol{q},\nu}(V)}{k_B T}\right]\right\} \quad (1)$$

where U is the internal energy, $\boldsymbol{q}$ is the wave vector, ν is the band index, $\omega_{\boldsymbol{q},\nu}$ is the phonon frequency at $\boldsymbol{q}$ and ν, T is temperature, and V is volume. The $\hbar$ and k_B are the reduced Planck constant and the Boltzmann constant, respectively. We determined the phonon frequencies, $\omega_{\boldsymbol{q},\nu}$, for all the unit-cell volumes explored in static DFT calculations. We explored temperatures from 0 K to 2000 K with an interval of 20 K. The volume dependence of the internal energy $U(V)$ is determined using the static DFT simulation as discussed. The zero point energy $\frac{1}{2}\sum_{\boldsymbol{q},\nu}\hbar\omega_{\boldsymbol{q},\nu}(V)$ and the thermal contributions $k_B T\sum_{\boldsymbol{q},\nu}\ln\{1\text{-}\exp[-\hbar\omega_{\boldsymbol{q},\nu}(V)/k_B T]\}$ constitute together the phonon contribution to Helmholtz free energy, defined as F_{phonon}. Thus, eq. (1) could also be expressed as:

$$F(V,T) = U(V) + F_{phonon}(V,T) \quad (2)$$

The phonon Helmholtz free energy F_{phonon} accounts for the volume dependence of phonon frequencies. The entropy (S) and heat capacity (C_V) at a constant volume are respectively calculated from its phonon density of states as functions of vibrational frequencies:

$$S = -\left(\frac{\partial F}{\partial T}\right)_V = -k_B \sum_{\boldsymbol{q},\nu} \ln\left\{1 - \exp\left[\frac{-\hbar\omega_{\boldsymbol{q},\nu}(V)}{k_B T}\right]\right\} - \frac{1}{T}\sum_{\boldsymbol{q},\nu} \frac{\hbar\omega_{\boldsymbol{q},\nu}(V)}{\exp\left[\frac{\hbar\omega_{\boldsymbol{q},\nu}(V)}{k_B T}\right]-1} \quad (3)$$

$$C_V = -T\left(\frac{\partial^2 F}{\partial T^2}\right)_V = \sum_{\boldsymbol{q},\nu} k_B \left[\frac{\hbar\omega_{\boldsymbol{q},\nu}(V)}{k_B T}\right]^2 \frac{exp\left[\frac{\hbar\omega_{\boldsymbol{q},\nu}(V)}{k_B T}\right]}{\left\{\exp\left[\frac{\hbar\omega_{\boldsymbol{q},\nu}(V)}{k_B T}\right]-1\right\}^2} \quad (4)$$

Our results on lattice parameters and elasticity are for a static lattice. To compare more directly with the room temperature experimental results on tremolite, we made corrections to the pressure via

198 $P = P_{static} + P_{phonon}$ (5)

199 where the P_{static} is related to $-[dU(V)/dV]$ and the P_{phonon} is determined from –
200 $[dF_{phonon}(V,T)/dV]_T$, where $U(V)$ and $F_{phonon}(V,T)$ are as defined in eq. (1) and (2).

201

202 **Results**

203 ***Equation of state and linear compressibility***

204 The energy as a function of unit-cell volume can be well described by the integral form
205 of a third-order Birch-Murnaghan equation of state (Birch, 1978) (**Figure 2**, **Supplementary**
206 **Figure 2**). The energy-volume results based on LDA yielded a zero-pressure unit-cell volume
207 V_0^{LDA} of 875.0 Å^3 and 887.1 Å^3 at 0 K and 300 K, respectively (**Table 1**). The prediction of
208 LDA at 300 K is 2.1% smaller than that based on single-crystal XRD study at ambient
209 conditions (Comodi et al., 1991). The corresponding GGA result is greater than the
210 experimental result by 5.8% (Comodi et al., 1991). The energy-volume results yielded a zero-
211 pressure bulk modulus (K_0^{LDA}) of 83.1 GPa and 78.5 GPa at 0 K and 300 K, respectively
212 (**Table 1**). The result at 300 K is in good agreement with the experimental result of 76±3 GPa
213 (Comodi et al., 1991; Comodi et al., 2010). The zero-pressure lattice parameters at 300 K are
214 also in excellent agreement with the experimental data (Comodi et al., 1991), differing from
215 the experimental data by no more than 1%. Specifically, a_0^{LDA} is smaller than a_0^{exp} by 0.6%,
216 b_0^{LDA} is smaller than b_0^{exp} by 0.9%, c_0^{LDA} is smaller than c_0^{exp} by 0.5%, and β_0^{LDA} is greater
217 than β_0^{exp} by 0.03%. To determine the incompressibility along individual directions, i.e., the
218 linear bulk moduli (K_l), where l= a-, b-, and c*-axes ($c^* = c\ sin\beta$), we used the dependence of
219 linear normalized pressure (F_l) on the linear finite strain (f_l), i.e., f_l -F_l relationships expressed
220 in terms of the K_l (Davies, 1974; Weaver, 1976; Meade and Jeanloz, 1990; Wentzcovitch and
221 Stixrude, 1997; Chheda et al., 2014) (**Table 1**, **Figure 2**):

222 $F_l = K_l + m_l f_l$ (6)

where the slope m_l is related to the pressure dependence of K_l and its particular value is not important in this study. The linear normalized pressure F_l could be further expressed in terms of the pressure (P), f_l, and the volume finite strain (f_V):

$$F_l = \frac{P}{f_l(1+2f_l)(1+2f_V)} \quad (7)$$

The linear finite strain f_l is related to the ratio of axial length (l) and the axial length at zero-pressure (l_0):

$$f_l = \frac{1}{2}\left(\left(\frac{l_0}{l}\right)^2 - 1\right) \quad (8)$$

The volume finite strain f_V is related to the ratio of unit-cell volume (V) and the unit-cell volume at zero-pressure (V_0):

$$f_V = \frac{1}{2}\left(\left(\frac{V_0}{V}\right)^{\frac{2}{3}} - 1\right) \quad (9)$$

The linear bulk moduli (K_l) are related to the bulk modulus (K_0) by $K_0 = (K_a^{-1}+K_b^{-1}+K_{c*}^{-1})^{-1}$ (Nye, 1985). Our results show consistency within 1.3%. The linear bulk moduli from both LDA and GGA indicate that tremolite is very anisotropic as documented by $K_a < K_{c*} < K_b$. We noted that LDA and GGA results bracket the experimental results, with LDA being in better agreement with the experimental data (**Table 1**, **Figure 2**).

Thermodynamic Parameters

We derived the fundamental thermodynamic parameters from the volume dependence of Helmholtz free energy at finite temperatures (Togo and Tanaka, 2015). The thermal expansion coefficient, α, is obtained from $(1/V)(\partial V/\partial T)_P$ (**Figure 3**). At 0 GPa and 300 K, we found $\alpha^{LDA} > \alpha^{GGA}$ with the former being 2.7×10^{-5} K^{-1} and the latter being 2.5×10^{-5} K^{-1}, respectively. The prediction from LDA is in better agreement with the experimental results of 3.13×10^{-5} K^{-1} on tremolite (Sueno et al., 1973). The source of discrepancy may lie in the fact that the experiments were conducted at only three temperatures, those being 24 °C, 400 °C,

and 700 °C. Our thermal expansion value based on LDA (α^{LDA}) is in very good agreement with the recent synchrotron XRD study on pargasite amphibole, which shows $2.7x10^{-5}$ K^{-1} at 300 K and 0 GPa (Comboni et al., 2017) (**Figure 3**). It should be noted that pargasite ($NaCa_2(Mg_4Al)(Si_6Al_2)O_{22}(OH)_2$) and tremolite are both calcic amphiboles. Upon compression, we noted that both α^{LDA} and α^{GGA} decreases (**Supplementary Table 4**).

One of the underlying assumptions about QHA is that minerals behave as harmonic solids et each volume, i.e., phonon frequencies depend only on volume, and heating at constant volume does not change the vibrational frequencies. This is true if the phonon modes are not interacting and this assumption often fails at higher temperatures (Oganov et al., 2002). The validity of QHA can be determined from the inflection point on the temperature dependence of the thermal expansion coefficient, beyond where $(\partial^2\alpha/\partial T^2)_P > 0$ at high temperatures (Wentzcovitch et al., 2004). However, it is very unlikely that tremolite will be thermodynamically stable at these temperatures, since it is known to dehydrate at ~1180 K and ~1 GPa, i.e., tremolite is likely to dehydrate before QHA limit is reached (Jenkins et al., 1991) (**Figure 3**).

Our predictions of specific heat capacity, C_P, at zero-pressure agree well with the existing experimental results (Krupka et al., 1985; Kahl and Maresch, 2001; Dachs et al., 2010). Our results at 300 K and 0 GPa for LDA and GGA are 660.0 $Jmol^{-1}K^{-1}$ and 675.4 $Jmol^{-1}K^{-1}$, respectively. In comparison, experimental results on tremolite are 658 $Jmol^{-1}K^{-1}$ (**Figure 3**) (Krupka et al., 1985; Kahl and Maresch, 2001; Dachs et al., 2010).

The Grüneisen parameter, γ, is defined as $\gamma = \alpha K_T V/C_V = \alpha K_S V/C_P$, where K_T and K_S are the isothermal and adiabatic bulk modulus, respectively. It decreases asymptotically as a function of temperature at zero-pressure (**Figure 3**). At low temperatures, the asymptotic behavior of the temperature dependence in γ is due to the fact that the temperature dependences of the thermodynamic parameters, i.e., α, K_T, and V, are smaller in magnitude

compared to that in the heat capacity, C_V. At high temperatures, the γ exhibits negligible temperature dependence (**Figure 3**). Previous studies indicate that γ is dependent on both temperature and volume and often exhibits non-monotonic temperature dependence (Oganov et al., 2000, 2002; Price et al., 1987). At 300 K, the numerical values of the γ^{LDA} and γ^{GGA} are 0.86 and 0.71, respectively. We also made independent estimates of γ from experimentally determined thermal parameters at 300 K and 0 GPa, i.e., α (Comboni et al., 2017), V and K_S (Brown and Abramson, 2016), and C_P (Dachs et al., 2010). The estimated γ ~0.95±0.07 is in good agreement with the LDA results (**Figure 3**). We further analyzed and discussed the thermoelastic parameters at simultaneous high temperatures and pressures (**Supplementary Section I**, **Supplementary Table 5**).

Crystal Structure at High-Pressure

We examined the crystal structure of tremolite as a function of volume. We explored volumes in both compressional and tensional regimes. Our results show that polyhedron volumes and bond lengths decrease upon compression (**Supplementary Table 6**). The pressure dependence of the volume of the polyhedral sites could be well described by a finite strain third-order Birch-Murnaghan equation of state (**Supplementary Table 7**). The zero-pressure volumes of the polyhedrons (V_0) are in good agreement with the experimental results based on single-crystal XRD (Comodi et al., 1991). However, the compressibilities of the polyhedral sites as estimated by experiments are not consistent with our results. This might be attributed to the fact that the crystal structure refinements from the single-crystal XRD were limited to two pressures at 0.0001 GPa and 3.5 GPa for tremolite. Therefore, it is likely that the polyhedral compressibilities were determined using linear fits of polyhedral volume and pressure (Comodi et al., 1991). Among the polyhedral units, the vacant A site is the softest and followed by the B site. The tetrahedral sites are the stiffest with $K_{T1} > K_{T2}$ while

297 the stiffness of octahedral sites is intermediate with $K_{M3} > K_{M1} > K_{M2}$ (**Supplementary Table**
298 **7**).
299
300 ***Elasticity***
301 Tremolite has 13 independent coefficients of the elastic tensor owing to its monoclinic
302 symmetry (Nye, 1985). In this section, we adopted the Voigt notation for the elastic tensor
303 (C_{ij}). So far only one experimental result on tremolite at ambient conditions has been reported
304 using impulsive stimulated light scattering method (Brown and Abramson, 2016). In their
305 measurements, the a^*-, b-, and c-axes of the crystal were aligned parallel to X-, Y-, and Z-
306 axes of the coordinate system, respectively, where $a^* = a \sin\beta$. However, in our simulations,
307 the unit-cell was only constrained with the b-axis parallel to the Y-axis. Thus we rotated the
308 experimentally determined elastic tensor by ~15° for better comparison (**Supplementary**
309 **Table 8**). The data show that our results based on LDA agree with the experimental data very
310 well (**Figure 4**, **Table 2**) (Brown and Abramson, 2016).
311 The principal coefficients of the elastic tensor stiffen upon compression, i.e., $dC_{ij}/dP > 0$,
312 and exhibit a relationship of $C_{22} > C_{33} > C_{11}$ over the pressure range of 0-10 GPa. The pressure
313 dependences of the principal coefficients are greater than those of other elastic coefficients,
314 including the off-diagonal and shear elastic coefficients. The shear coefficients C_{66}, based on
315 LDA results, decreases upon compression, i.e., $dC_{66}/dP < 0$. The results based on GGA show
316 that the C_{66} initially increases ($dC_{66}/dP > 0$) and then decreases ($dC_{66}/dP < 0$) upon
317 compression with an inflection point at a pressure of ~6 GPa (**Figure 4**). It is likely that such
318 an inflection point occurs for LDA at a larger volume, i.e., a negative pressure, and it is not
319 sampled in our study. The errors in the coefficients of the elastic tensor are within 0.4%
320 except for the shear off-diagonal coefficients (C_{15}, C_{25}, C_{35}, C_{46}) which have errors within
321 4.1%. The absolute errors in the shear off-diagonal coefficients are <0.06 GPa. The Voigt-

Reuss-Hill average bulk (K_{VRH}) and shear (G_{VRH}) moduli increase with pressure. We noted that the $G' < K'$, because all shear coefficients (C_{44}, C_{55}, C_{66}) have systematically lower pressure dependences than those of the principal and off-diagonal coefficients, i.e., C_{11}, C_{22}, C_{33}, C_{23}, C_{31}, and C_{12}. The errors in the elastic moduli are within 0.1%. Similarly, the compressional wave velocity (V_P) increases at a faster rate with pressure. Based on LDA results, the shear wave velocity (V_S) initially increases but then decreases at ~8 GPa. Compared to the changes in the compressional wave velocity, shear wave velocity is rather insensitive to pressure (**Figure 5**). The errors of the velocities are within 0.04%. Eulerian finite strain formalism adequately explains the pressure dependence of the coefficients of the elastic tensor (**Table 2**) (Chheda et al., 2014; Karki et al., 2001).

Anisotropy

Based upon the linear compressibilities and the coefficients of the elastic tensor, it is clear that tremolite is very anisotropic. We determined the seismic velocities of tremolite along different propagation directions using the Christoffel equation (Mainprice, 1990):

$$\det|T_{ik} - \delta_{ik}\rho V_x^2| = 0 \quad (10)$$

where δ_{ik} is the Kronecker delta, V_x is the seismic velocity, where x= {P, S1, S2}, P refers to the compressional wave and S1 and S2 refer to fast and slow shear waves, respectively, and T_{ik} is the Christoffel stiffness. The T_{ik} for a certain propagation direction is defined by:

$$T_{ik}(\boldsymbol{n}) = C_{ijkl}\boldsymbol{n_j n_l} \quad (11)$$

where the C_{ijkl} is the coefficients of the elastic tensor with the full notation and $\boldsymbol{n_j n_l}$ are the direction cosines.

The anisotropy AV_x is defined by:

$$AV_x = \frac{V_x^{max} - V_x^{min}}{\frac{1}{2}(V_x^{max} + V_x^{min})} \times 100\% \quad (12)$$

where V_x^{max} and V_x^{min} are respectively the maximum and minimum velocities solved from Eq. (10), where x= {P, S}, and S refers to the shear wave.

We determined the elastic anisotropy for both LDA and GGA results and compared them with the recent experimental study (Brown and Abramson, 2016). Stereographic projections show that our results agree well with the experimental results (**Figure 6**). Upon compression, the compressional wave velocity anisotropy (AV_P) decreases while shear wave velocity anisotropy (AV_S) increases. The pressure dependent behavior of AV_S is likely to be related to the negative pressure dependence of C_{66}, since the other coefficients of the elastic tensor stiffen upon compression. At 0 GPa and 300 K, AV_P^{LDA} is 34.6% and AV_S^{LDA} is 27.5%. At 3 GPa corresponding to the thermodynamic stability of tremolite, AV_P^{LDA} reduces to 29.5%, i.e., by 14.7%. In contrast, AV_S^{LDA} increases to 30.8%, i.e., by 12.0%. At 10 GPa, the maximum pressure explored in this study, AV_P^{LDA} reduces to 22.6%, while AV_S^{LDA} increases to 38.8% (**Supplementary Table 9**).

Discussion

The pressure dependence of the elastic properties could be better understood in terms of the evolution of the crystal structure under pressure. For instance, among the principal coefficients of the elastic tensor, the finding that $C_{22} > C_{33} > C_{11}$ could be explained in terms of the I-beam units that constitute the crystal structure of tremolite (**Figure 1**). The I-beam is connected to adjacent I-beams via A and B cations, which are weaker linkages. Along the *b*-axis, i.e., [010] direction, three adjacent I-beams are linked by a B site. Along the *a*-axis, i.e., [100] direction, I-beams are connected by an A site. In tremolite, the A sites are vacant allowing for a further weakening of the I-beam linkages. The pressure-induced evolution of the I-beams shape could be well understood in terms of the distances between the basal oxygen pairs. The distance of O7-O7' and O4-O4' along the *a*-axis indicate the inner and

outer thickness of I-beam, respectively (**Supplementary Figure 3**). The difference between inner and outer thicknesses indicates the bending of the I-beam. At room pressures, the I-beam is bent with a concave curvature whereas under compression, owing to the greater compressibility of the vacant A site, there is a reduction in the bend, i.e., the concave curvature of the I-beam. There is an inflection in the bend curvature to a convex shape at further compression to pressures of ~10 GPa (**Supplementary Figure 3**). Similar to I-beam thickness, we could also quantify the separation between two adjacent I-beams. One can further distinguish between the inner and outer separations, as determined by the distance of O7-O7'' and O4-O4'' along the *a*-axis, respectively (**Supplementary Figure 3**). Because of the difference in the compressibility of the A and B sites, the distance of O4-O4'' varies little while the distance of O7-O7'' decreases about 0.7 Å from 0 to 10 GPa. Based on LDA results, we noted that the O4-O4'' initially decreases but then increases, leading to a change in the shape of the I-beam. Hence, the bending of the I-beam along the *a*-axis appears to be crucial in explaining the finding that C_{11} is softer compared to C_{22} and C_{33}.

Since individual tetrahedral units are quite stiff, they could be treated as effectively rigid bodies and the crystal structure responds to compression by rotation of the tetrahedral units. The tetrahedral rotation angle indicates the extent to which the ditrigonal ring deviates from a regular hexagon, and is defined by $\theta = (\sum^{6}_{i=1}|\phi_i - 120°|)/12$, where ϕ_i is the angle between three adjacent basal oxygen atoms (**Supplementary Figure 3**). Based on results from LDA, we noted that θ increases from 6.5° at room pressure to 10.3° at 10 GPa (**Supplementary Figure 3**). The increase in θ could be rationalized in terms of the greater stiffness along the *b*-axis compared to the *c*-axis. Thus, the finding that $C_{22} > C_{33}$ could be rationalized in terms of the behavior of θ upon compression.

The elastic anisotropy of tremolite can also be understood in terms of the behavior of the individual structural units. For instance, the compressional wave (V_P) and the fast shear

wave (V_{S1}) are relatively faster along *b*- and *c**-axes forming a girdle perpendicular to the *a*-axis. The slow shear wave (V_{S2}) is faster along the *c**-axis (**Figure 6**). This is likely to be related to the stiffer I-beam and its weaker linkages along the *a*-axis.

It is well known that sheet silicates exhibit large elastic anisotropy that persists to lower crustal/upper mantle depths (Jiang et al., 2006; Mainprice et al., 2008; Bezacier et al., 2010; Chheda et al., 2014; Mookherjee and Mainprice, 2014). In contrast, amphibole is elastically less anisotropic, but owing to its greater thermal stability, is often more abundant in deep crustal and upper mantle lithologies. Thus amphibole is also likely to play an important role in explaining the seismic anisotropy of lower crustal and/or upper mantle lithologies that have experienced a deformation (Tatham et al., 2008; Ji et al., 2013).

The crystal structure of tremolite ($Ca_2Mg_5Si_8O_{22}(OH)_2$), a double chain silicate, can be considered as a hybrid crystal structure of talc ($Mg_6Si_8O_{20}(OH)_4$ for 2 formula units), a sheet silicate, and diopside ($Ca_4Mg_4Si_8O_{24}$ for 4 formula units), a single chain silicate. Based on the existing literature data and our results, we found that the thermodynamic and elastic properties of tremolite (tr) are intermediate between those of diopside (di) and talc (tlc). For instance, at ambient conditions, $(\alpha_T K_T)^{di}$ (2.18×10^{-3} GPa/K) > $(\alpha_T K_T)^{tr}$ (2.12×10^{-3} GPa/K) > $(\alpha_T K_T)^{tlc}$ (1.23×10^{-3} GPa/K) (Isaak et al., 2006; Ulian and Valdrè, 2015). The heat capacity C_P of tremolite (660.1 $Jmol^{-1}K^{-1}$) is intermediate between that of diopside (666.9 $Jmol^{-1}K^{-1}$) and talc (650.8 $Jmol^{-1}K^{-1}$) (Krupka et al., 1985). The elastic properties also exhibit a similar trend, i.e., the isothermal bulk modulus K_T of tremolite (78.5 GPa) is intermediate between that of diopside (109.1 GPa) and talc (55.1 GPa) (Zhao et al., 1998; Ulian and Valdrè, 2015). The isothermal bulk moduli, K_T, for all the mineral phases are from a third-order Birch-Murnaghan equation of state. Similarly, the shear elastic moduli *G* of tremolite (58.1 GPa) is in between that of diopside (72.8 GPa) and talc (39.7 GPa) (Isaak et al., 2006; Ulian et al., 2014).

421

422 **Implication**

423 Metamorphosed ultramafic rocks and calc-silicate rocks could be examined in a CaO-
424 MgO-SiO_2-H_2O-CO_2 (CMSHC) system (Spear, 1993). In these metamorphosed rocks,
425 tremolite is likely to be stable over a wide range of pressures (~0-3 GPa), temperatures
426 (~400-900 °C), and chemistries (Spear, 1993; Jenkins et al., 1991). The presence of tremolite
427 means that an ultramafic or calc-silicate mineral assemblage has experienced intermediate
428 pressures (Spear, 1993). In contrast, the presence of talc in the mineral assemblage indicates
429 that the assemblage has equilibrated at a lower metamorphic grade while diopside indicates
430 equilibration at a relatively higher one. In fact, the gradual change of talc to tremolite to
431 diopside with increasing pressure and temperature, i.e., metamorphic grade, has been well
432 documented in siliceous dolomitic marbles in the Lepontine Alps (Trommsdorff, 1970;
433 Winter, 2010) (**Figure 7**). We compiled the velocity-density systematics for a series of
434 minerals, including talc, tremolite, and diopside, that are likely to be stable in the CMSHC
435 system and found a strong correlation between the density and seismic velocity of all the
436 minerals in CMSHC system. In metamorphosed/ metasomatized regions that are not exposed
437 in an outcrop, such velocity-density systematics will be valuable in constraining the extent of
438 metamorphism/metasomatism (**Figure 7**).

439 To evaluate whether metasomatism could explain the anomalously low seismic velocity
440 at MLD depths, we compared the shear wave velocity of a nonmetasomatized lithology with
441 that of metasomatized ones. For determining the velocity-depth profile for the
442 nonmetasomatized lithology, we used the mineral assemblage and geotherm (surface heat
443 flow of 40, 45, and 50 mW/m^2) representative of a typical craton, the Kaapvaal Craton
444 (Griffin et al., 2009; Artemieva, 2009) (**Supplementary Table 10**). To constrain the degree
445 of metasomatism, we modeled metasomatized lithologies by varying the modal abundances

446 of amphibole between 5 and 25% at the depths of 70-90 km, i.e., MLD depths. We also
447 incorporated 1 vol% of phlogopite throughout the entire modeled depth range, i.e., 50-200
448 km. We calculated the velocity-depth profiles for these metasomatized lithologies by using
449 the thermoelastic codes (Abers and Hacker, 2016) (**Figure 8**). Details of the thermoelastic
450 formalisms and parameters used for our calculations for the anhydrous mantle mineral phases
451 can be found in the supplementary information (**Supplementary Section II**, **Supplementary**
452 **Table 11**). We updated the thermoelastic parameters for the hydrous minerals and used those
453 of tremolite from this study as a proxy for amphiboles that are likely to be stable in
454 metasomatized lithologies (**Table 3**). We defined the velocity reduction as $\Delta V_S = (V_S^{Ref} -$
455 $V_S^{Meta})/V_S^{Ref}$ x 100% at a given depth, where the V_S^{Ref} is the reference velocity for the
456 nonmetasomatized lithology, and V_S^{Meta} is the velocity for the metasomatized lithology
457 containing hydrous phases, i.e., amphiboles and phlogopite. We found that ΔV_S is sensitive to
458 the degree of metasomatism. For instance, for a geotherm with the surface heat flow of 45
459 mW/m^2, 5 vol% of amphibole can account for a V_S reduction of only 0.02 km/s, or ΔV_S of
460 0.4%. In contrast, 25 vol% of amphibole can account for a V_S reduction of 0.09 km/s, or 1.9%.
461 In addition to 25 vol% of amphibole, another 1 vol% of phlogopite leads to a further
462 reduction of 0.02 km/s, i.e., a total of 0.11 km/s or 2.3% reduction. We also found that the
463 ΔV_S is rather insensitive to the choice of geotherm (**Figure 8**). However, it is sensitive to the
464 choice of thermoelastic parameters for the hydrous minerals. For instance, parameters
465 tabulated in the existing thermoelastic database (Abers and Hacker, 2016) significantly
466 overestimate the velocity reduction (**Table 3**, **Figure 8**). For the same degree of
467 metasomatism and a geotherm with 45 mW/m^2 surface heat flow, the thermoelastic
468 parameters from the earlier database (Abers and Hacker, 2016) suggest that 25 vol% of
469 amphibole can account for a V_S reduction of 0.18 km/s, or ΔV_S of 3.8%; an addition of 1 vol%
470 phlogopite leads to a further reduction of 0.03 km/s, i.e., a total of 0.20 km/s or 4.4%

reduction (**Figure 8**). Previous estimates with similar modal abundances of amphibole and phlogopite accounted for a shear wave velocity reduction of >5% (Selway et al., 2015). The geophysically observed reduction in V_S ranges from 3 to 10% (Lekić and Fischer, 2014; Sodoudi et al., 2013; Wölbern et al., 2012; Savage and Silver, 2008). Thus, we found the presence of amphibole and phlogopite associated with metasomatism could account for some reduction of V_S but may not be the sole mechanism responsible for MLD. However, it is to be noted that our estimates of the V_S for amphibole are based on alkali (K/Na) and iron (Fe) free tremolite end members. Recent estimates show that iron- and alkali-bearing end members could further reduce shear wave velocity (V_S) by another 0.1 km/s per atom of alkali or iron in the formula unit (Brown and Abramson, 2016). However, the pressure and temperature dependences on elastic properties of the amphibole solid solution remain unknown and would be important for providing better constraints on their role at MLD depths. In addition to mantle metasomatism, other proposed mechanisms might also be required to explain the MLD, such as elastically accommodated grain boundary sliding (Karato et al., 2015; Karato and Park, 2019) and/or the presence of partial melts (Fischer et al., 2010).

Acknowledgements

The authors thank two anonymous reviewers and the Associate Editor Dr. Sergio Speziale for their thorough reviews and constructive comments which enhanced the clarity of the manuscript. The authors would like to acknowledge Aaron Ashley, Dr. Suraj Bajgain for their comments which improved the manuscript. This work is supported by the US National Science Foundation grant EAR 1763215 and EAR 1753125. The authors acknowledge computing resources from the High Performance Computing, Research Computing Center, Florida State University and from the NSF Extreme Science and Engineering Discovery Environment (XSEDE) (TG-GEO170003).

496

497 **References:**

498 Abers, G.A., and Hacker, B.R. (2016) A MATLAB toolbox and Excel workbook for
499 calculating the densities, seismic wave speeds, and major element composition of
500 minerals and rocks at pressure and temperature. Geochemistry, Geophysics,
501 Geosystems, 17, 616-624.

502 Abt, D.L., Fischer, K.M., French, S.W., Ford, H.A., Yuan, H., and Romanowicz, B. (2010)
503 North American lithospheric discontinuity structure imaged by P_S and S_P receiver
504 functions. Journal of Geophysical Research: Solid Earth, 115, 1-24.

505 Anderson, O.L., Isaak, D., and Oda, H. (1992) High-temperature elastic constant data on
506 minerals relevant to geophysics. Reviews of Geophysics, 30, 57-90.

507 Artemieva, I.M. (2009) The continental lithosphere: reconciling thermal, seismic, and
508 petrologic data. Lithos, 109, 23-46.

509 Bailey, E., and Holloway, J.R. (2000) Experimental determination of elastic properties of talc
510 to 800 C, 0.5 GPa; calculations of the effect on hydrated peridotite, and implications for
511 cold subduction zones. Earth and Planetary Science Letters, 183, 487-498.

512 Baroni, S., De Gironcoli, S., Dal Corso, A., and Giannozzi, P. (2001) Phonons and related
513 crystal properties from density-functional perturbation theory. Reviews of Modern
514 Physics, 73, 515.

515 Bezacier, L., Reynard, B., Bass, J.D., Sanchez-Valle, C., and Van de Moortèle, B. (2010)
516 Elasticity of antigorite, seismic detection of serpentinites, and anisotropy in subduction
517 zones. Earth and Planetary Science Letters, 289, 198-208.

518 Birch, F. (1978) Finite strain isotherm and velocities for single crystal and polycrystalline
519 NaCl at high-pressures and 300 K. Journal of Geophysical Research, 83, 1257-1268.

520 Brown, J.M., and Abramson, E.H. (2016) Elasticity of calcium and calcium-sodium
521 amphiboles. Physics of the Earth and Planetary Interiors, 261, 161-171.
522 Carlson, R.W., Pearson, D.G., and James, D.E. (2005) Physical, chemical, and chronological
523 characteristics of continental mantle. Reviews of Geophysics, 43, 1-24.
524 Ceperley, D.M., and Adler, B.J. (1980) Ground state of the electron gas by a stochastic
525 method. Physical Review Letters, 45, 566-569.
526 Chen, C.C., Lin, C.C., Liu, L.G., Sinogeikin, S.V., and Bass, J.D. (2001) Elasticity of single-
527 crystal calcite and rhodochrosite by Brillouin spectroscopy. American Mineralogist, 86,
528 1525-1529.
529 Chen, P.F., Chiao, L.Y., Huang, P.H., Yang, Y.J., and Liu, L.G. (2006) Elasticity of
530 magnesite and dolomite from a genetic algorithm for inverting Brillouin spectroscopy
531 measurements. Physics of the Earth and Planetary Interiors, 155, 73-86.
532 Chheda, T., Mookherjee, M., Mainprice, D., dos Santos, A.M., Molaison, J.J., Chantel, J.,
533 Manthilake, G., and Bassett, W.A. (2014) Structure and elasticity of phlogopite under
534 compression: Geophysical implications. Physics of the Earth and Planetary Interiors,
535 233, 1-12.
536 Cline II, C.J., Faul, U.H., David, E.C., Berry, A.J., and Jackson, I. (2018) Redox-influenced
537 seismic properties of upper-mantle olivine. Nature, 555, 355-358.
538 Comboni, D., Lotti, P., Gatta, G.D., Merlini, M., Liermann, H.P., and Frost, D.J. (2017)
539 Pargasite at high pressure and temperature. Physics and Chemistry of Minerals, 45,
540 259-278.
541 Comodi, P., Ballaran, T.B., Zanazzi, P.F., Capalbo, C., Zanetti, A., Nazzareni, S. (2010) The
542 effect of oxo-component on the high-pressure behavior of amphiboles. American
543 Mineralogist, 95, 1042-1051.

544 Comodi, P., Mellini, M., Ungaretti, L., and Zanazzi, P.F. (1991) Compressibility and high
545 pressure structure refinement of tremolite, pargasite, and glaucophane. European
546 Journal of Mineralogy, 3, 485-499.
547 Dachs, E., Baumgartner, I.A., Bertoldi, C., Benisek, A., Tippelt, G., and Maresch, W.V.
548 (2010) Heat capacity and third-law entropy of kaersutite, pargasite, fluoropargasite,
549 tremolite and fluorotremolite. European Journal of Mineralogy, 22, 319-331.
550 Davies, G.F. (1974) Effective elastic moduli under hydrostatic stress—I. quasi-harmonic
551 theory. Journal of Physics and Chemistry of Solids, 35, 1513-1520.
552 Fischer, K.M., Ford, H.A., Abt, D.L., and Rychert, C.A. (2010) The lithosphere-
553 asthenosphere boundary. Annual Review of Earth and Planetary Science, 38, 551-575.
554 Frost, D.J. (2006) The stability of hydrous mantle phases. Reviews in Mineralogy and
555 Geochemistry, 62, 243-271.
556 Gajdoš, M., Hummer, K., Kresse, G., Furthmüller, J., and Bechstedt, F. (2006) Linear optical
557 properties in the projector-augmented wave methodology. Physical Review B, 73,
558 045112.
559 Griffin, W.L., O'reilly, S.Y., Afonso, J.C., and Begg, G.C. (2009) The composition and
560 evolution of lithospheric mantle: a re-evaluation and its tectonic implications. Journal
561 of Petrology, 50, 1185-1204.
562 Gung, Y., Romanowicz, B., and Panning, M. (2003) Global anisotropy and the thickness of
563 continents. Nature, 422, 707-711.
564 Hacker, B.R., and Abers, G.A. (2004) Subduction Factory 3: An Excel worksheet and macro
565 for calculating the densities, seismic wave speeds, and H_2O contents of minerals and
566 rocks at pressure and temperature. Geochemistry, Geophysics, Geosystems, 5,
567 Q01005, doi:10.1029/2003GC000614.

568 Hohenberg, P., and Kohn, W. (1964) Inhomogenous electron gas. Physical Review B, 136,
569 B864-871.
570 Isaak, D.G., Ohno, I., and Lee, P.C. (2006) The elastic constants of monoclinic single-crystal
571 chrome-diopside to 1,300 K. Physics and Chemistry of Minerals, 32, 691-699.
572 Jackson, J.M., Sinogeikin, S.V., and Bass, J.D. (2007) Sound velocities and single-crystal
573 elasticity of orthoenstatite to 1073 K at ambient pressure. Physics of the Earth and
574 Planetary Interiors, 161, 1-12.
575 Jenkins, D.M., Corona, J.C., Bassett, W.A., Mibe, K., and Wang, Z. (2010) Compressibility
576 of synthetic glaucophane. Physics and Chemistry of Minerals, 37, 219-226.
577 Jenkins, D.M., Holland, T.J., and Clare, A.K. (1991) Experimental determination of the
578 pressure-temperature stability field and thermochemical properties of synthetic
579 tremolite. American Mineralogist, 76, 458-469.
580 Ji, S., Shao, T., Michibayashi, K., Long, C., Wang, Q., Kondo, Y., Zhao, W., Wang, H., and
581 Salisbury, M.H. (2013) A new calibration of seismic velocities, anisotropy, fabrics, and
582 elastic moduli of amphibole-rich rocks. Journal of Geophysical Research: Solid Earth,
583 118, 4699-4728.
584 Jiang, F., Speziale, S., and Duffy, T.S. (2006) Single-crystal elasticity of brucite, $Mg(OH)_2$,
585 to 15 GPa by Brillouin scattering. American Mineralogist, 91, 1893-1900.
586 Kahl, W.A., and Maresch, W.V. (2001) Enthalpies of formation of tremolite and talc by high-
587 temperature solution calorimetry-a consistent picture. American Mineralogist, 86,
588 1345-1357.
589 Karato, S.I., and Park, J. (2019) On the origin of the upper mantle seismic discontinuities. In
590 Lithospheric Discontinuities, edited by Yuan, H. and Romanovicz, B., 5-34.
591 Karato, S.I., Olugboji, T., and Park, J. (2015) Mechanisms and geologic significance of the
592 mid-lithosphere discontinuity in the continents. Nature Geoscience, 8, 509-514.

Karki, B.B., Stixrude, L., and Wentzcovitch, R.M. (2001) Elastic properties of major materials of earth's mantle from first principles. Reviews of Geophysics, 39, 507-534.

Kohn, W., and Sham, L.J. (1965) Self-consistent equations including exchange and correlation effects. Physical Review, 140, 1133-1138.

Kresse, G., and Furthmüller, J. (1996a) Efficiency of ab-initio total energy calculations for metals and semiconductors using a plane-wave basis set. Computational Material Science, 6, 15-50.

Kresse, G., and Furthmüller, J. (1996b) Efficient iterative schemes for ab initio total-energy calculations using a plane-wave basis set. Physical Review B, 54, 11169-11186.

Kresse, G., and Hafner, J. (1993) Ab initio molecular-dynamics for liquid-metals. Physical Review B, 47, 558-561.

Kresse, G., and Joubert, D. (1999) From ultrasoft pseudopotentials to the projector augmented-wave method. Physical Review B, 59, 1758-1775.

Krupka, K.M., Hemingway, B.S., Robie, R.A., and Kerrick, D.M. (1985) High-temperature heat capacities and derived thermodynamic properties of anthophyllite, diopside, dolomite, enstatite, bronzite, talc, tremolite and wollastonite. American Mineralogist, 70, 261-271.

Lekić, V., and Fischer, K.M. (2014) Contrasting lithospheric signatures across the western United States revealed by S_P receiver functions. Earth and Planetary Science Letters, 402, 90-98.

Lundqvist, S., and March, N.H. (1987) Theory of the inhomogeneous electron gas. Plenum Press, New York.

Mainprice, D. (1990) An efficient FORTRAN program to calculate seismic anisotropy from the lattice preferred orientation of minerals. Computational Gesoscience, 16, 385-393.

Mainprice, D., Le Page, Y., Rodgers, J., and Jouanna, P. (2008) Ab initio elastic properties of talc from 0 to 12 GPa: interpretation of seismic velocities at mantle pressures and prediction of auxetic behaviour at low pressure. Earth and Planetary Science Letters, 274, 327-338.

Mandler, B.E., and Grove, T.L. (2016) Controls on the stability and composition of amphibole in the Earth's mantle. Contributions to Mineralogy and Petrology, 171, 68.

Mao, Z., Fan, D., Lin, J.F., Yang, J., Tkachev, S.N., Zhuravlev, K., and Prakapenka, V.B. (2015) Elasticity of single-crystal olivine at high pressures and temperatures. Earth and Planetary Science Letters, 426, 204-215.

Meade, C., and Jeanloz, R. (1990) Static compression of $Ca(OH)_2$ at room temperature: observations of amorphization and equation of state measurements to 10.7 GPa. Geophysical Research Letters, 17, 1157-1160.

Mittal, V., Jiang, Z., Silber, R.E., Girard, J., and Karato, S.I. (2019) Some issues on the role of Ti-H on the physical properties of olivine. AGU Fall Meeting 2019.

Monkhorst, H.J., and Pack, J.D. (1976) Special points for Brillouin-zone integrations. Physical Review B, 13, 5188-5192.

Mookherjee, M., and Bezacier, L. (2012) The low velocity later in subduction zone: structure and elasticity of glaucophane at high pressures. Physics of the Earth and Planetary Interiors, 208-209, 50-58.

Mookherjee, M., and Mainprice, D. (2014) Unusually large shear wave anisotropy for chlorite in subduction zone settings. Geophysical Research Letters, 41, 1506-1513.

Mookherjee, M., Mainprice, D., Maheshwari, K., Heinonen, O., Patel, D., and Hariharan, A. (2016) Pressure induced elastic softening in framework aluminosilicate-albite ($NaAlSi_3O_8$). Scientific Reports, 6, 34815.

Mookherjee, M., Panero, W., Wunder, B., and Jahn, S. (2019) Anomalous elastic behavior of phase Egg, $AlSiO_3(OH)$, at high pressures. American Mineralogist, 104, 130-139.

Nestola, F., Pasqual, D., Welch, M.D., and Oberti, R. (2012) The effects of composition upon the high-pressure behaviour of amphiboles: compression of gedrite to 7 GPa and a comparison with anthophyllite and proto-amphibole. Mineralogical Magazine, 76, 987-995.

Nye, J.F. (1985) Physical properties of crystals. Oxford University Press, Clarendon.

Oganov, A.R., Brodholt, J., and Price, G.D. (2000) Comparative study of quasiharmonic lattice dynamics, molecular dynamics and Debye model in application to $MgSiO_3$ perovskite. Physics of the Earth and Planetary Interiors, 122, 277-288.

Oganov, A.R., Brodholt, J., and Price, G.D. (2002) Ab initio theory of phase transitions and thermoelasticity of minerals. In EMU Notes in Mineralogy, in Energy Modelling in Minerals, edited by Gramaccioli, C.M., 4, 83–170. Eötvös University Press, Budapest.

Ohno, I., Harada, K., and Yoshitomi, C. (2006) Temperature variation of elastic constants of quartz across the α-β transition. Physics and Chemistry of Minerals, 33, 1-9.

Peng, Y., Mookherjee, M., Hermann, A., Bajgain, S., Liu, S., and Wunder, B. (2017) Elasticity of Phase-Pi ($Al_3Si_2O_7(OH)_3$)-A hydrous aluminosilicate phase. Physics of the Earth and Planetary Interiors, 269, 91-97.

Perdew, J.P., and Wang, Y. (1986) Accurate and simple density functional for the electronic exchange energy: generalized gradient approximation. Physical Review B, 33, 8800–8802.

Perdew, J.P., Chevary, J.A., Vosko, S.H., Jackson, K.A., Pederson, M.R., Singh, D.J., and Fiolhais, C. (1992) Atoms, molecules, solids, and surfaces: applications of the generalized gradient approximation for exchange and correlation. Physical Review B, 46, 6671-6687.

Price, G.D., Parker, S.C., and Leslie, M. (1987) The lattice dynamics and thermodynamics of the Mg_2SiO_4 polymorphs. Physics and Chemistry of Minerals, 15, 181-190.

Rychert, C.A., and Shearer, P.M. (2009) A Global View of the Lithosphere-Asthenosphere Boundary. Science, 324, 495-498.

Rychert, C.A., Fischer, K.M., and Rondenay, S. (2005) A sharp lithosphere–asthenosphere boundary imaged beneath eastern North America. Nature, 436, 542-545.

Saha, S., Dasgupta, R., and Tsuno, K. (2018) High Pressure Phase Relations of a Depleted Peridotite Fluxed by CO_2-H_2O-Bearing Siliceous Melts and the Origin of Mid-Lithospheric Discontinuity. Geochemistry, Geophysics, Geosystems, 19, 595-620.

Savage, B., and Silver, P.G. (2008) Evidence for a compositional boundary within the lithospheric mantle beneath the Kalahari craton from S receiver functions. Earth and Planetary Science Letters, 272, 600-609.

Selway, K., Ford, H., and Kelemen, P. (2015) The seismic mid lithosphere discontinuity. Earth and Planetary Science Letters, 414, 45-57.

Sodoudi, F., Yuan, X., Kind, R., Lebedev, S., Adam, J.M.C., Kästle, E., and Tilmann, F. (2013) Seismic evidence for stratification in composition and anisotropic fabric within the thick lithosphere of Kalahari Craton. Geochemistry, Geophysics, Geosystems, 14, 5393-5412.

Spear, F.S. (1993) Metamorphic phase equilibria and pressure-temperature-time paths. Mineralogical Society of America Monograph, 799, Washington, DC.

Stixrude, L., Cohen, R.E., and Hemley, R.J. (1998) Theory of minerals at high pressure. Reviews of Mineralogy, 37, 639-670.

Sueno, S., Cameron, M., Papike, J.J., and Prewitt, C.T. (1973) The high temperature crystal chemistry of tremolite. American Mineralogist, 58, 649-664.

690 Tatham, D.J., Lloyd, G.E., Butler, R.W.H., and Casey, M. (2008) Amphibole and lower
691 crustal seismic properties. Earth and Planetary Sciences Letters, 267, 118-128.
692 Togo, A., and Tanaka, I. (2015) First principles phonon calculations in material science.
693 Scripta Materiala, 108, 1-5.
694 Trommsdorff, V. (1970) Mineral paragenesis in magnesian rocks of the progressive
695 metamorphic series of the central Alps. Naturwissenschaften, 57, 304-305.
696 Tulk, C.A., Gagnon, R. E., Kiefte, H., and Clouter, M. J. (1994) Elastic constants of ice III by
697 Brillouin spectroscopy. Journal of Chemical Physics, 101, 2350-2354.
698 Tutti, F., Dubrovinsky, L.S., and Nygren, M. (2000) High-temperature study and thermal
699 expansion of phlogopite. Physics and Chemistry of Minerals, 27, 599-603.
700 Ulian, G., and Valdrè, G. (2015) Density functional investigation of the thermophysical and
701 thermochemical properties of talc [$Mg_3Si_4O_{10}(OH)_2$]. Physics and Chemistry of
702 Minerals, 42, 151-162.
703 Ulian, G., Tosoni, S., and Valdrè, G. (2014) The compressional behaviour and the
704 mechanical properties of talc [$Mg_3Si_4O_{10}(OH)_2$]: a density functional theory
705 investigation. Physics and Chemistry of Minerals, 41, 639-650.
706 Weaver, J.S. (1976) Application of finite strain theory to non-cubic crystals. Journal of
707 Physics and Chemistry of Solids, 37, 711-718.
708 Welch, M.D., Gatta, G.D., and Rotiroti, N. (2011) The high-pressure behavior of
709 orthorhombic amphiboles. American Mineralogist, 96, 623-630.
710 Wentzcovitch, R.M., and Stixrude, L. (1997) Crystal chemistry of forsterite: A first-
711 principles study. American Mineralogist, 82, 663-671.
712 Wentzcovitch, R.M., Karki, B.B., Cococcioni, M., and De Gironcoli, S. (2004) Thermoelastic
713 Properties of $MgSiO_3$-Perovskite: Insights on the Nature of the Earth's Lower Mantle.
714 Physical Review Letters, 92, 018501.

715 Winter J.D. (2010) Principles of Igneous and Metamorphic Petrology. Prentice Hall, New
716 York.
717 Wölbern, I., Rümpker, G., Link, K., and Sodoudi, F. (2012) Melt infiltration of the lower
718 lithosphere beneath the Tanzania craton and the Albertine rift inferred from S receiver
719 functions. Geochemistry, Geophysics, Geosystems, 13, Q0AK08,
720 doi:10.1029/2012GC004167.
721 Yang, H., and Evans, B.W. (1996) X-ray structure refinements of tremolite at 140 and 295 K:
722 Crystal chemistry and petrologic implications. American Mineralogist, 81, 1117-1125.
723 Yang, H., Hazen, R.M., Prewitt, C.T., Finger, L.W., Lu, R., and Hemley, R.J. (1998) High-
724 pressure single-crystal X-ray diffraction and infrared spectroscopic studies of the C2/m-
725 $P2_1/m$ phase transition in cummingtonite. American Mineralogist, 83, 288-299.
726 Yuan, H., Romanowicz, B. (2019) Introduction-Lithospheric Discontinuities, In Lithospheric
727 Discontinuities, edited by Yuan, H. and Romanovicz, B., 1-3.
728 Zanazzi, P.F., Nestola, F., and Pasqual, D. (2010) Compressibility of protoamphibole: A
729 high-pressure single-crystal diffraction study of protomangano-ferro-anthophyllite.
730 American Mineralogist, 95, 1758-1764.
731 Zha, C.S., Mao, H.K., and Hemley, R.J. (2000) Elasticity of MgO and a primary pressure
732 scale to 55 GPa. Proceedings of National Academy of Sciences USA, 97, 13494-13499.
733 Zhang, L., Ahsbahs, H., Kutoglu, A., and Hafner, S.S. (1992) Compressibility of grunerite.
734 American Mineralogist, 77, 480-483.
735 Zhao, Y., and Von Dreele, R.B., Zhang, J.Z., and Weidner, D.J. (1998) Thermoelastic
736 equation of state of monoclinic pyroxene: $CaMgSi_2O_6$ diopside. The Review of High
737 Pressure Science and Technology, 7, 25-27.
738

739 **Figure Caption**

Figure 1: Crystal structure of tremolite amphibole predicted using *first principles* simulation at ~3 GPa. (**a**) Projection along the (001) plane: the crystal structure consists of tetrahedral units (SiO_4) forming double chains and octahedral units (MgO_6) arranged to form strips. The octahedral strip is sandwiched between two tetrahedral double chains with their apices pointing towards each other, together forming an I-beam denoted by bold black dashed lines. Large B sites are occupied by Ca and are located at the edge of the octahedral strip. The hydroxyl groups (OH) are located at the center of the strips of octahedral units. (**b**) Projection along the (100) plane: the crystal structure shows the tetrahedral double chains and the octahedral strips extend in the [001] direction. Also shown are the mirror (dashed black lines), the 2-fold axis (gray ellipse with a line), and the unit-cell edge (a continuous black line) for reference.

Figure 2: (**a**) Helmholtz free energy vs. unit-cell volume for tremolite amphibole. The open circles indicate unit-cell volume at zero-pressure. The experimentally unit-cell volume V_0^{Exp} is indicated by a green shaded bar (Comodi et al., 1991). (**b**) Pressure vs. unit-cell volume for tremolite amphibole at 300 K. (**c**-**e**) Lattice parameters: *a*-; *b*-; *c*-axes vs. pressure at 300 K. Inset shows the plot of lattice parameter β vs. pressure. (**f**-**h**) Linear normalized pressure, F_l, vs. linear Eulerian finite strain, f_l, at 300 K for *a*-, *b*-, and *c**-axis, respectively. The vertical intercepts indicate the linear compressibility: K_a, K_b, and K_{c*} (**Table 1**). The error bars for the normalized pressure are estimated to be ±0.1 GPa based on the numerical precision of the calculations determined from the convergence of total energy (**Supplementary Table 1**, **2**). Legend: LDA: pink symbols; GGA: light blue symbols; and experimental results (Exp): green symbols (Comodi et al., 1991).

Figure 3: (**a**) Thermal expansion coefficient (α) of tremolite as a function of temperature at zero-pressure. The filled blue circle refers to α of tremolite at ambient conditions

765 (Sueno et al., 1973). The filled orange circle represents α of pargasite experimentally
766 determined at ambient conditions from a synchrotron XRD study (Comboni et al.,
767 2017). Note that tremolite is an end member composition of pargasitic amphibole. (**b**)
768 Specific heat capacity (C_P) as a function of temperature at zero-pressure. The
769 experimental results are also at ambient pressure (Krupka et al., 1985; Kahl and
770 Maresch, 2001; Dachs et al., 2010). (**c**) Grüneisen parameter (γ) as a function of
771 temperature at zero-pressure. The black triangle represents γ determined using the
772 equation $\gamma = \alpha V K_S / C_P$, where thermodynamic parameters are from previous
773 experimental studies: α (Comboni et al., 2017), V and K_S (Brown and Abramson,
774 2016), and C_P (Dachs et al., 2010) at ambient conditions. The solid and dashed lines
775 in the panel (**a-c**) represent the properties at temperatures where QHA is valid and
776 invalid, respectively. The Debye temperature and the thermodynamic stability are
777 indicated by the pink and green shaded bars, respectively.

778 **Figure 4**: (**a**) Comparison between the coefficients of the elastic tensor predicted from *first*
779 *principles* simulations in this study and experimental results at ambient conditions
780 (BA16: Brown and Abramson, 2016). (**b-e**) Coefficients of the elastic tensor, C_{ij}, of
781 tremolite as a function of pressure at 300 K: (**b**) the principal coefficients, C_{11}, C_{22},
782 and C_{33}; (**c**) the shear coefficients, C_{44}, C_{55}, and C_{66}; (**d**) the off-diagonal coefficients,
783 C_{23}, C_{13}, and C_{12}; and (**e**) the shear off-diagonal coefficients, C_{15}, C_{25}, C_{35}, and C_{46}.

784 **Figure 5**: (**a**) Bulk (K_{VRH}) and shear (G_{VRH}) moduli as functions of pressure at 300 K. The
785 subscript VRH refers to the Hill average of the Voigt and Reuss Bounds. The inset
786 shows the isothermal bulk moduli as a function of temperature at zero-pressure. The
787 purple circle is the bulk modulus (Reuss limit) derived from the experimentally-
788 determined elastic tensor (BA16: Brown and Abramson, 2016). The green circle
789 represents the isothermal bulk modulus determined by a second-order Birch-

Murnaghan equation of state (C91: Comodi et al., 1991). The solid and dashed lines represent the isothermal bulk moduli at temperatures where QHA is valid and invalid, respectively. (**b**) Compressional (V_P) and shear (V_S) wave velocity as a function of pressure at 300 K. Purple symbols in all panels refer to experimental results (BA16: Brown and Abramson, 2016).

Figure 6: Comparison of seismic anisotropy of tremolite between this study (averages of LDA and GGA) and an experimental study (Brown and Abramson, 2016) at ambient conditions. The stereographic projections down the *c*-axis are shown for (**a**) V_P, (**b**) V_{S1}, and (**c**) V_{S2} from this study and (**d**) V_P, (**e**) V_{S1}, and (**f**) V_{S2} from the experiment.

Figure 7: (**a**) Ternary composition diagram of the system CaO-MgO-SiO_2-H_2O-CO_2 (CMSHC), projected from H_2O and CO_2. Such a ternary system is representative of both metamorphosed ultramafic rocks (black symbols) and calc-silicates rocks (white symbols). Mineral phases stable in both lithologies are shown as half-black and half-white circles. The inset depicts the metamorphic zones showing diopside (Di), tremolite (Tr), and talc (Tlc) as indicator minerals in regionally metamorphosed dolomitic marbles of the Lepontine Alps, along the Swiss-Italian border (Trommsdorff, 1970; Winter, 2010). (**b**) Velocities as a function of density for mineral phases in the CMSHC system. Inset shows the velocities as a function of water content for diopside (Di), tremolite (Tr), and talc (Tlc). The water content is also shown in (**a**) by the bar with a blue gradient. Legend: compressional (V_P) and shear (V_S) wave velocity are represented by circles and squares in (**b**), respectively, and their corresponding trends are shown as dashed lines. The mineral abbreviations and references: antigorite (Atg) (Bezacier et al., 2010), brucite (Brc) (Jiang et al., 2006), calcite (Cal) (Chen et al., 2001), diopside (Di) (Isaak et al., 2006), dolomite (Dol) (Chen et al., 2006), enstatite (En) (Jackson et al., 2007), forsterite (Fo) (Mao et

al., 2015), ice (Ice-III) (Tulk et al., 1994), periclase (Per) (Zha et al., 2000), quartz (Qtz) (Ohno et al., 2006), talc (Tlc) (Ulian et al., 2014), and tremolite (Tr) (this study).

Figure 8: Shear wave velocity-depth profiles for lithospheric mantle assemblages based on geotherms with varying surface heat flows of (**a**) 40 mW/m^2; (**b**) 45 mW/m^2; and (**c**) 50 mW/m^2. The reference (nonmetasomatized) lithology is based on the Kaapvaal Craton composition (**Supplementary Table 10**) (Griffin et al., 2009). The degree of mantle metasomatism and its effect on V_S is modeled by varying abundances of amphiboles (amp) (solid colored lines) between 70-90 km depth. Throughout the entire depth range displayed, an additional 1 vol% of phlogopite (phl) (dashed lines) is incorporated in the metasomatized lithology, following earlier work (Selway et al., 2015). The solid black lines indicate the velocity-depth profiles of the reference (nonmetasomatized) lithology (V_S^{ref}). Thermoelastic data for hydrous phases are reported in **Table 3**. AH16: velocity-depth profiles calculated using the thermoelastic database (Abers and Hacker, 2016); S15 (Selway et al., 2015), since the reference velocity-depth profile was not reported, we assumed a baseline (orange dashed lines) and recalculated the shear wave velocity reduction. Hence, it is to be noted that the ΔV_S of ~3.6% for S15 does not account for the effect of 1% phlogopite on velocity reduction. Lower panels represent plots of the ΔV_S caused by incorporating amphibole (and phlogopite) based on geotherms with varying surface heat flows of (**d**) 40 mW/m^2; (**e**) 45 mW/m^2; and (**f**) 50 mW/m^2. The pink shaded areas indicate the reported MLD ΔV_S of 3-5%. In some regions, the reduction is >10% and is not shown in this diagram.

This is a preprint, the final version is subject to change, of the American Mineralogist (MSA)
Cite as Authors (Year) Title. American Mineralogist, in press.
DOI: https://doi.org/10.2138/am-2020-7189

Table 1. Equation of state and lattice parameters for tremolite.

E_0 [eV]	V_0 [Å^3]	K_0 [GPa]	K'	a_0 [Å]	K_a [GPa]	b_0 [Å]	K_b [GPa]	c_0* [Å]	K_{c*} [GPa]	T [K]	Method
-647.8	875.0	83.1	6.6	9.708	168.2	17.83	391.8	5.056	294.5	0	LDA[a]
-587.7	945.4	68.3	6.2	10.02	143.4	18.24	341.7	5.176	215.4	0	GGA[a]
-641.0	887.1	78.5	5.2	9.776	157.3	17.88	406.0	5.076	266.8	300	LDA[a]
-581.3	958.4	66.3	6.1	10.08	137.8	18.29	356.1	5.199	201.3	300	GGA[a]
-	905.76	76	4	9.840	-	18.042	-	5.102	-	300	SCXRD[b]

[a] *this study*
[b] Comodi et al., 1991: SCXRD: single-crystal X-ray diffraction. The bulk modulus (K_0) determined by a quadratic fitting of volume with pressure in Comodi et al., 1991 is 85 GPa, and is updated to 76±3 GPa using a second-order Birch-Murnaghan equation of state in Comodi et al., 2010.

This is a preprint, the final version is subject to change, of the American Mineralogist (MSA)
Cite as Authors (Year) Title. American Mineralogist, in press.
DOI: https://doi.org/10.2138/am-2020-7189

Table 2a. Pressure dependence of the elastic constants (C_{ij}), bulk (K), and shear (G) moduli for tremolite using LDA. The finite strain fit results and their pressure derivatives are also tabulated.

V [Å^3]	$P_{0\,K}$ [GPa]	$P_{300\,K}$ [GPa]	ρ [g/cm^3]	C_{11} [GPa]	C_{22} [GPa]	C_{33} [GPa]	C_{12} [GPa]	C_{13} [GPa]	C_{23} [GPa]	C_{44} [GPa]	C_{55} [GPa]	C_{66} [GPa]	C_{15} [GPa]	C_{25} [GPa]	C_{35} [GPa]	C_{46} [GPa]	K_{VRH} [GPa]	G_{VRH} [GPa]
LDA (PAW)																		
800	10.00	10.62	3.37	181.0	249.6	249.5	84.1	110.6	89.2	88.0	87.7	43.9	2.1	0.6	-19.9	11.0	137.1	66.4
810	8.27	9.05	3.33	171.4	242.0	240.5	79.9	103.3	83.4	87.5	85.5	44.6	0.6	0.1	-21.1	9.9	130.2	65.6
820	6.69	7.58	3.29	162.2	234.9	231.9	75.8	96.2	78.1	86.9	83.4	45.6	-1.0	-0.5	-22.4	8.9	123.6	65.0
830	5.23	6.22	3.25	153.1	227.8	223.6	71.9	89.1	73.0	86.2	81.1	46.2	-2.6	-1.1	-23.7	8.0	117.1	64.1
840	3.89	4.94	3.21	144.4	221.2	215.6	68.1	82.4	68.4	85.3	78.9	46.8	-4.3	-1.6	-24.9	7.2	110.9	63.1
850	2.66	3.75	3.17	136.1	214.8	208.0	64.7	75.5	63.9	84.4	76.6	47.2	-6.0	-2.3	-26.2	6.3	104.8	62.2
860	1.53	2.65	3.14	128.1	208.2	200.3	61.5	69.3	59.6	83.3	74.3	47.5	-7.6	-3.0	-27.5	5.5	98.9	61.0
870	0.49	1.61	3.10	120.9	202.2	192.9	58.3	63.0	55.5	82.1	71.8	47.7	-9.1	-3.8	-28.9	4.8	93.3	59.9
880	-0.46	0.65	3.07	114.2	195.8	186.2	55.1	56.5	51.7	80.9	69.4	47.9	-10.6	-4.6	-30.3	4.0	87.6	58.9
890	-1.33	-0.25	3.03	108.1	189.8	179.3	52.3	51.0	48.2	79.5	66.8	47.8	-11.9	-5.4	-31.8	3.2	82.4	57.6
finite strain fit at 0 K																		
875.0	0	1.12	3.08	117.6	198.8	189.6	56.6	59.9	53.6	81.5	70.6	47.8	-9.8	-4.2	-29.6	4.3	90.3	59.4
first pressure derivative				7.3	6.4	7.3	3.2	6.4	4.0	1.3	2.6	-0.1	1.6	0.8	1.4	0.8	5.7	1.2
second pressure derivative				-0.3	-0.4	-0.4	-0.1	-0.4	-0.1	-0.2	-0.2	-0.1	-0.1	-0.1	-0.1	0.0	-0.2	-0.1
finite strain fit at 300 K																		
887.1	-1.09	0	3.04	109.4	191.5	181.2	53.1	52.6	49.1	80.0	67.6	47.9	-11.6	-5.1	-31.3	3.5	83.8	58.0
first pressure derivative				7.4	6.6	7.6	3.2	6.6	4.0	1.4	2.7	0.0	1.7	0.9	1.5	0.8	5.9	1.3
second pressure derivative				-0.2	-0.3	-0.3	-0.1	-0.3	-0.1	-0.2	-0.2	-0.1	-0.1	-0.1	-0.1	0.0	-0.2	-0.1

This is a preprint, the final version is subject to change, of the American Mineralogist (MSA)
Cite as Authors (Year) Title. American Mineralogist, in press.
DOI: https://doi.org/10.2138/am-2020-7189

Table 2b. Pressure dependence of the elastic constants (C_{ij}), bulk (K), and shear (G) moduli for tremolite amphibole using GGA. The finite strain fit results and their pressure derivatives are also tabulated.

V [Å^3]	$P_{0\,K}$ [GPa]	$P_{300\,K}$ [GPa]	ρ [g/cm^3]	C_{11} [GPa]	C_{22} [GPa]	C_{33} [GPa]	C_{12} [GPa]	C_{13} [GPa]	C_{23} [GPa]	C_{44} [GPa]	C_{55} [GPa]	C_{66} [GPa]	C_{15} [GPa]	C_{25} [GPa]	C_{35} [GPa]	C_{46} [GPa]	K_{VRH} [GPa]	G_{VRH} [GPa]
GGA (PAW)																		
860	8.66	9.97	3.14	156.4	222.0	217.0	72.0	89.9	74.4	83.7	77.9	45.1	-1.5	-1.4	-23.6	5.6	117.0	62.3
880	6.11	7.33	3.07	142.2	209.6	202.8	65.4	77.9	65.9	81.8	73.9	45.6	-4.1	-2.6	-25.6	4.1	106.1	60.5
900	3.92	5.05	3.00	128.5	197.8	190.1	59.3	66.9	58.4	79.5	69.8	45.7	-6.6	-3.9	-27.6	2.6	95.9	58.5
920	2.03	3.07	2.93	117.1	186.9	178.3	53.9	56.4	51.9	77.0	65.5	45.4	-8.8	-5.3	-29.7	1.3	86.5	56.4
940	0.40	1.37	2.87	107.7	176.8	168.9	48.7	46.7	46.9	74.4	61.2	45.0	-10.7	-6.7	-31.7	-0.1	78.1	54.4
960	-1.00	-0.11	2.81	99.8	167.5	161.9	43.8	38.1	43.2	71.6	56.5	44.3	-12.2	-8.1	-33.7	-1.3	70.8	52.3
finite strain fit at 0 K																		
945.4	0.00	0.95	2.85	105.4	174.2	167.0	47.3	44.5	46.2	73.6	59.8	44.8	-11.0	-7.1	-32.3	-0.4	76.1	53.7
first pressure derivative				6.0	6.6	6.1	3.4	6.2	3.0	1.9	3.1	0.4	1.2	1.0	1.4	0.9	5.3	1.4
second pressure derivative				0.0	-0.4	-0.1	-0.2	-0.3	0.1	-0.2	-0.3	-0.1	0.0	-0.1	-0.1	-0.1	-0.1	-0.1
finite strain fit at 300 K																		
958.4	-0.90	0.00	2.81	100.0	168.2	161.4	44.2	38.8	43.0	71.8	57.0	44.3	-12.2	-8.0	-33.5	-1.2	71.2	52.5
first pressure derivative				5.7	6.6	5.9	3.3	6.2	2.8	2.0	3.2	0.5	1.2	1.0	1.4	0.9	5.2	1.4
second pressure derivative				0.0	-0.4	-0.1	-0.2	-0.3	0.1	-0.3	-0.3	-0.1	0.0	-0.1	-0.1	-0.1	-0.1	-0.1

This is a preprint, the final version is subject to change, of the American Mineralogist (MSA)
Cite as Authors (Year) Title. American Mineralogist, in press.
DOI: https://doi.org/10.2138/am-2020-7189

Table 3. Thermoelastic data for tremolite (tr) and phlogopite (phl).

phase	gram formula weight (g/mol)	molar volume (cm^3/mol)	density @298K (kg/m^3)	wt% H_2O	expansivity (/K)	isothermal bulk modulus (Pa)	dK_T/dP	shear modulus (Pa)	dlnG/dlnρ	dG/dP	first Grüneisen parameter	second Grüneisen parameter	Reference
	gfw	V	ρ_{298}	H_2O	a^0	K_T	K_T'	G	Γ	G'	γ_{th}	δ_T	
tr	812.37	267.13	3041	2.20	4.94E-05[1]	7.85E+10	5.19	5.80E+10	3.33[2]	1.27	0.86	3.33[3]	*ref*[a]
tr	812.37	272.70	2979	2.20	5.34E-05	8.50E+10	4.00	5.05E+10	4.79	0.99	0.79	4.79	*ref*[b]
phl	417.24	149.31	2794	4.50	7.60E-05[d][1]	5.12E+10	9.10	3.66E+10	11.73[2]	1.83	0.56[e]	11.73[f][4]	*ref*[c]
phl	417.24	149.70	2788	4.50	5.79E-05	4.97E+10	8.59	2.70E+10	9.18	0.91	0.59	9.18	*ref*[b]

ref[a]: *This study,* using parameters based on LDA.
ref[b]: Abers and Hacker, 2016, and the references or notes therein.
ref[c]: Chheda et al., 2014, data represented here are the average of LDA and GGA.
ref[d]: Tutti et al., 2000.
ref[e]: Ulian and Valdrè, 2015, talc is used as a proxy for phlogopite which has a very similar crystal structure.
ref[f]: Bailey and Holloway, 2000, talc is used as a proxy for phlogopite.
Note [1]: The expansivity constant a^0 is obtained by fitting V vs. T.
Note [2]: The parameter Γ is approximated as $\Gamma = \delta_T$ (Anderson et al., 1992; Hacker and Abers, 2004) when G vs. T is not known.
Note [3]: The isothermal second Grüneisen parameter δ_T is obtained by fitting K_T vs. T.
Note [4]: The isothermal second Grüneisen parameter δ_T is obtained based on its definition formula.
For the details about the parameters, please refer to the Supplementary Information (**Supplementary Section II**).

This is a preprint, the final version is subject to change, of the American Mineralogist (MSA)
Cite as Authors (Year) Title. American Mineralogist, in press.
DOI: https://doi.org/10.2138/am-2020-7189

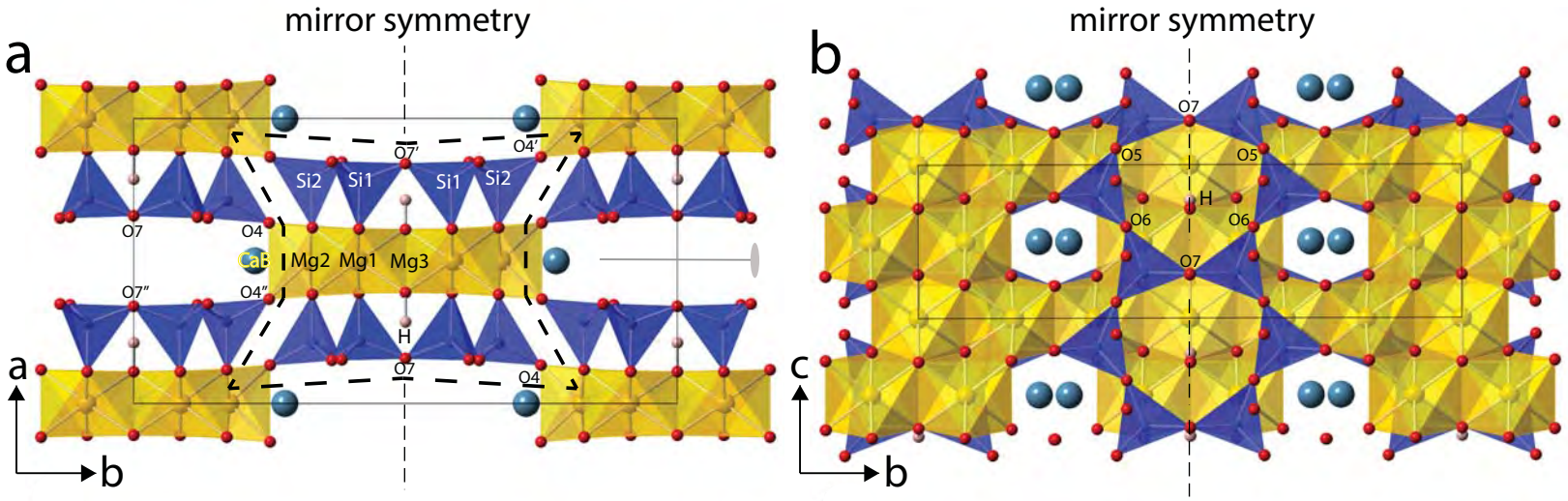

Figure 1

This is a preprint, the final version is subject to change, of the American Mineralogist (MSA)
Cite as Authors (Year) Title. American Mineralogist, in press.
DOI: https://doi.org/10.2138/am-2020-7189

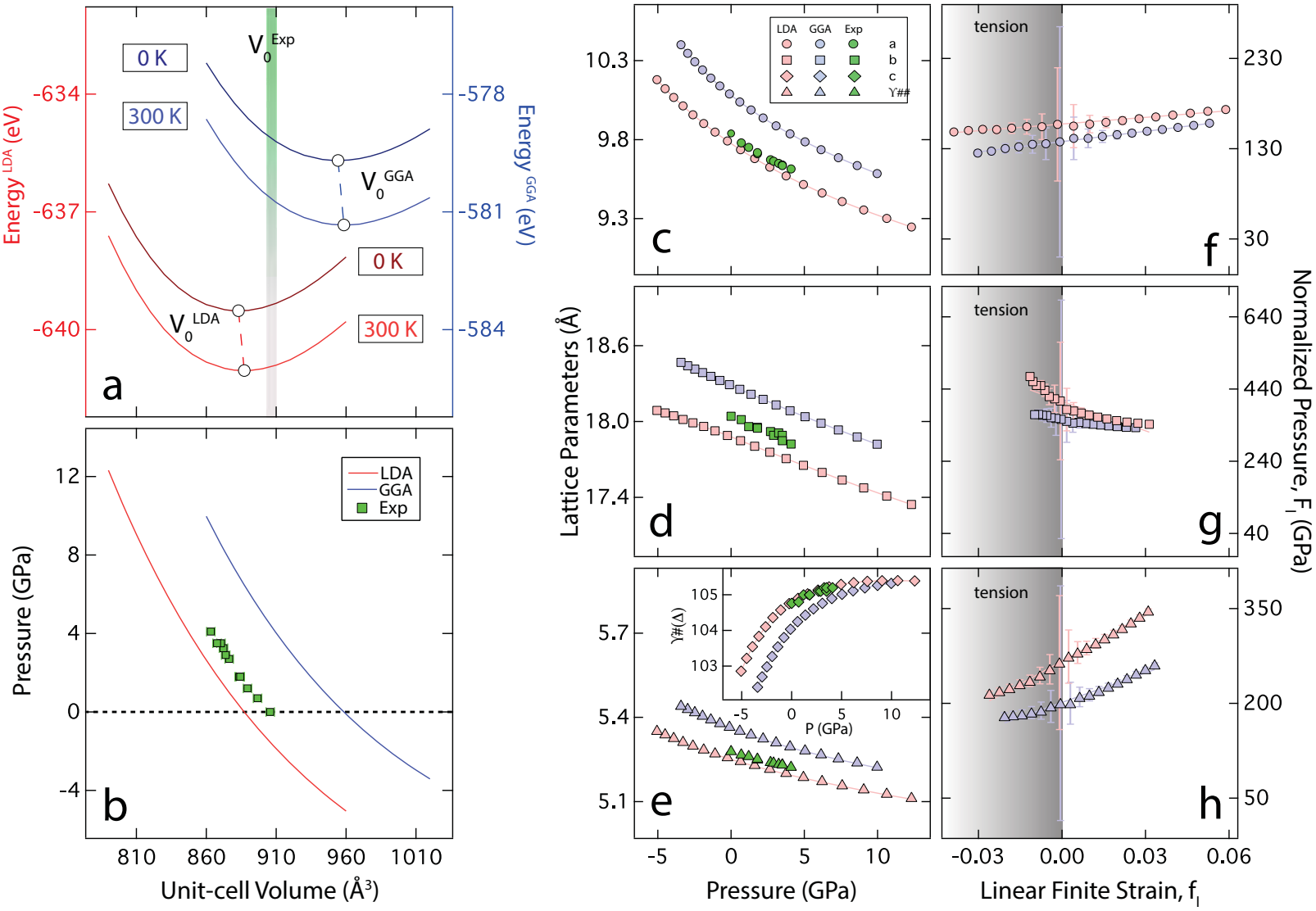

Figure 2

This is a preprint, the final version is subject to change, of the American Mineralogist (MSA)
Cite as Authors (Year) Title. American Mineralogist, in press.
DOI: https://doi.org/10.2138/am-2020-7189

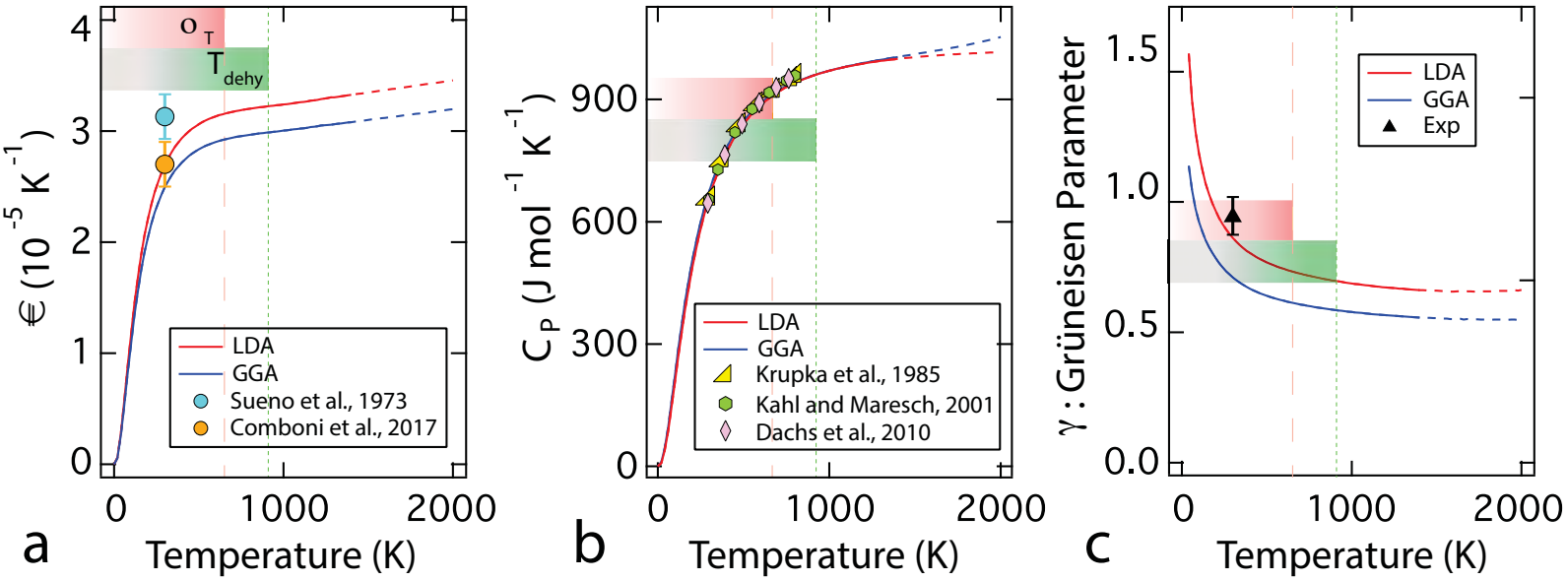

Figure 3

This is a preprint, the final version is subject to change, of the American Mineralogist (MSA)
Cite as Authors (Year) Title. American Mineralogist, in press.
DOI: https://doi.org/10.2138/am-2020-7189

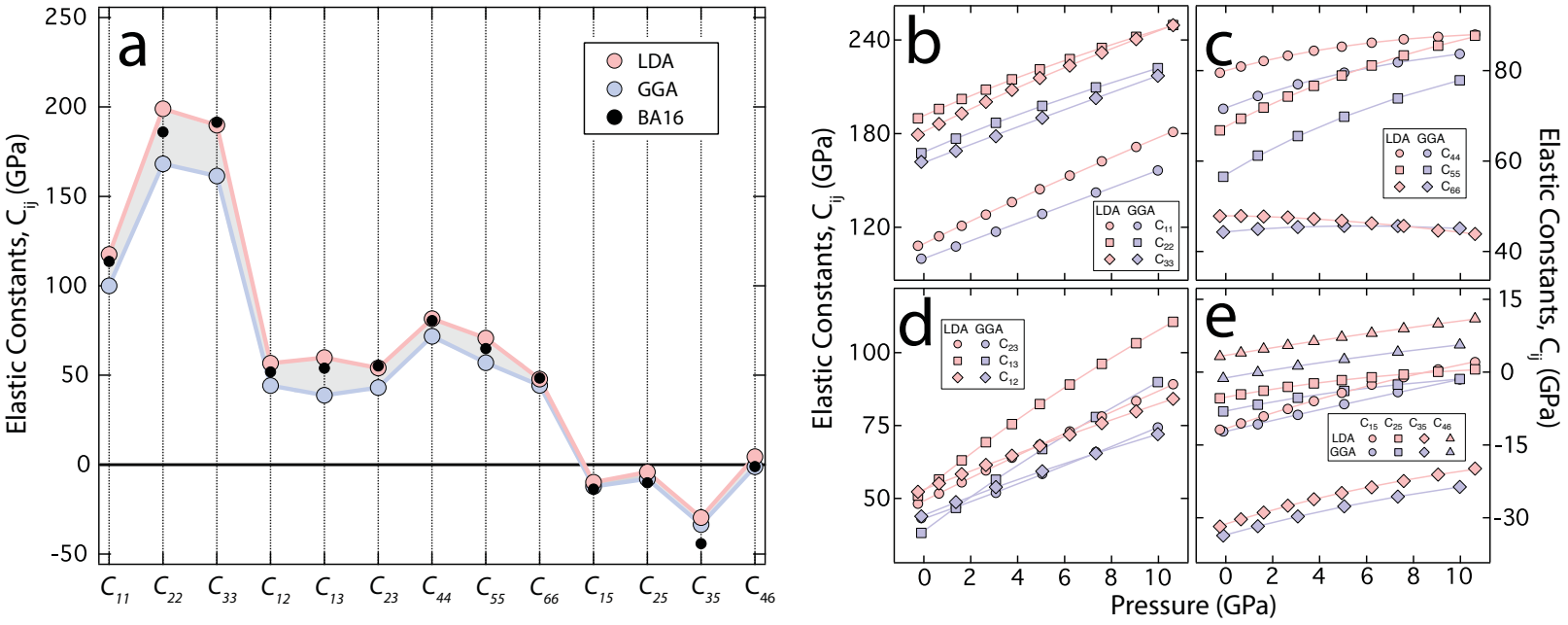

Figure 4

This is a preprint, the final version is subject to change, of the American Mineralogist (MSA)
Cite as Authors (Year) Title. American Mineralogist, in press.
DOI: https://doi.org/10.2138/am-2020-7189

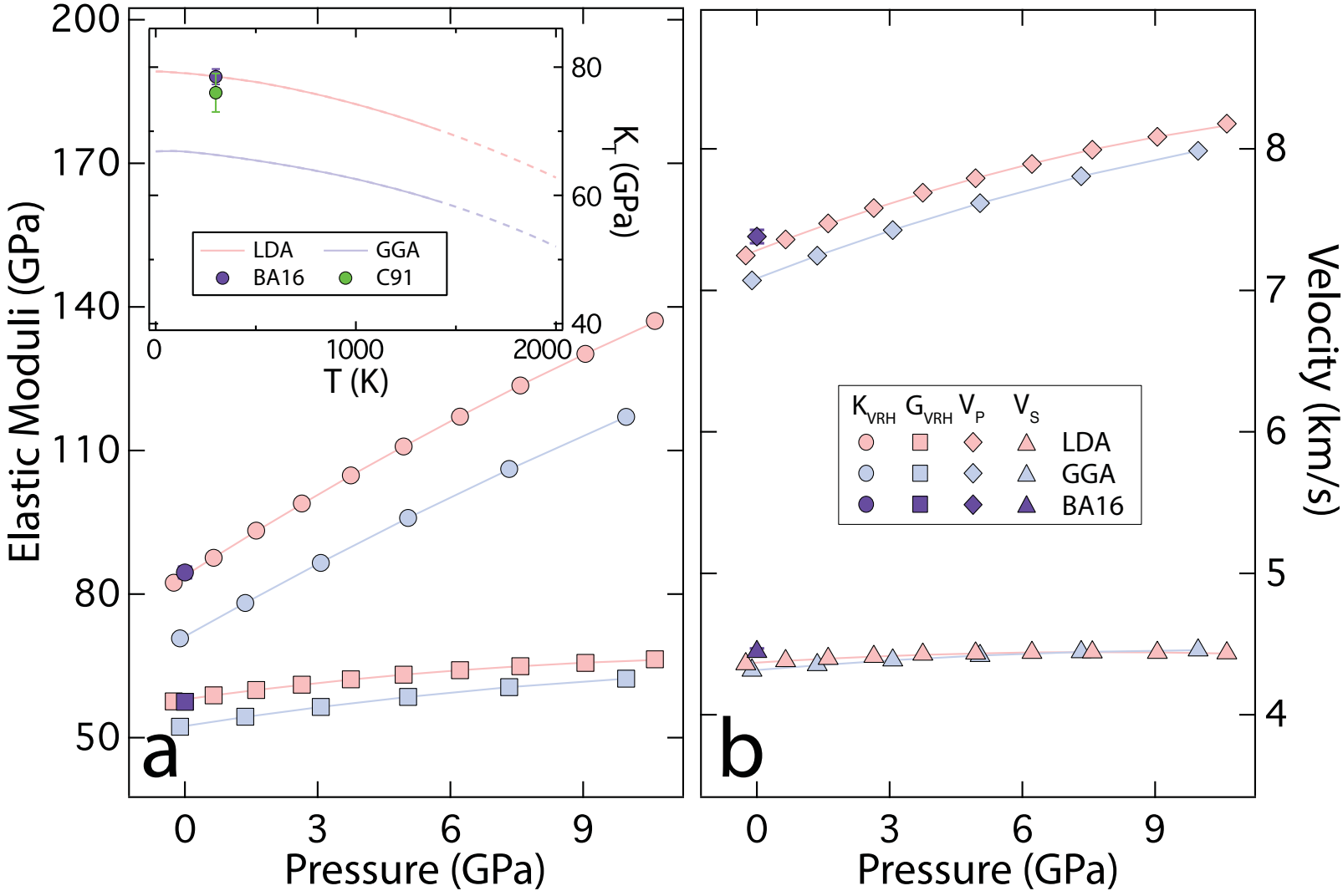

Figure 5

This is a preprint, the final version is subject to change, of the American Mineralogist (MSA)
Cite as Authors (Year) Title. American Mineralogist, in press.
DOI: https://doi.org/10.2138/am-2020-7189

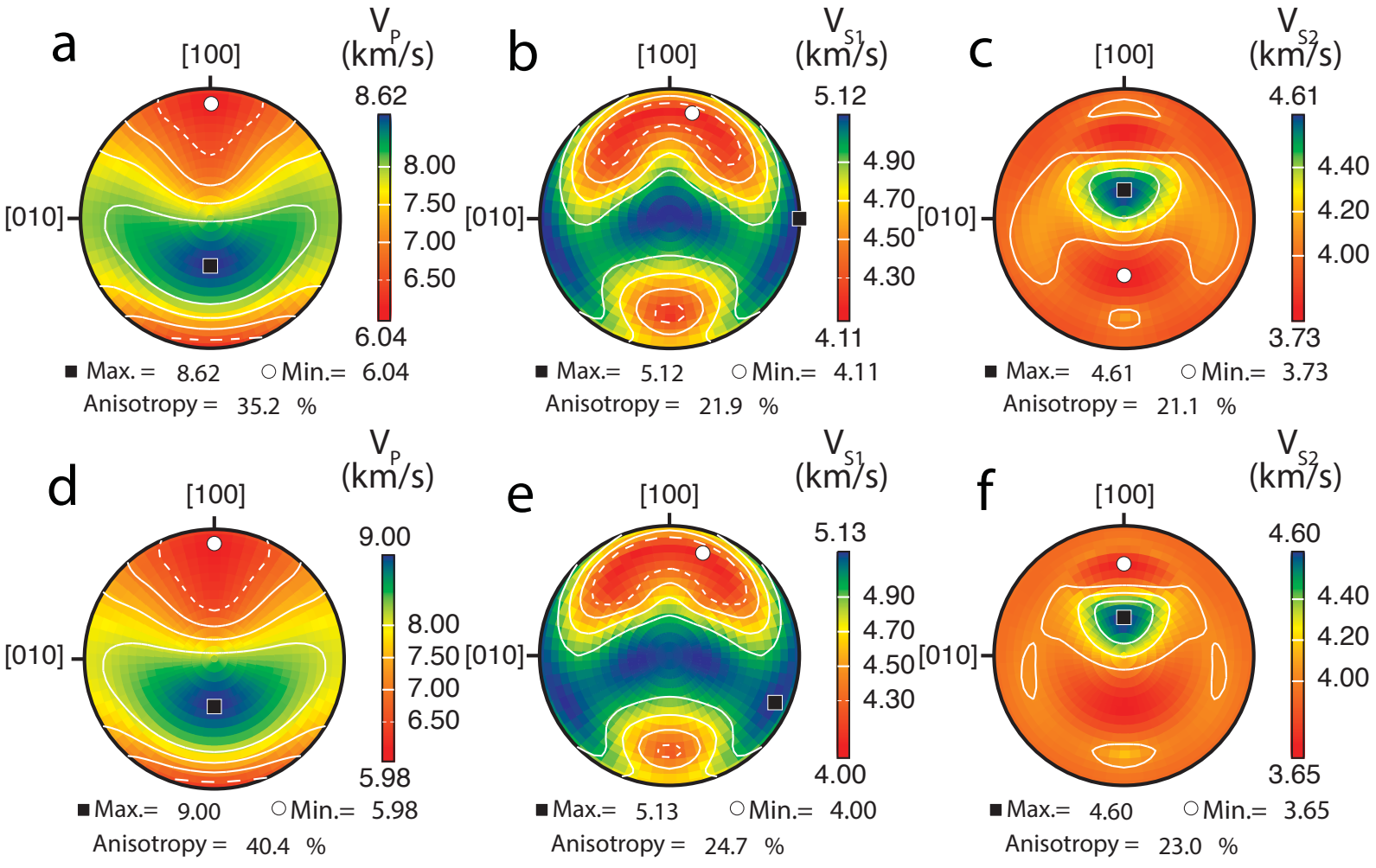

Figure 6

This is a preprint, the final version is subject to change, of the American Mineralogist (MSA)
Cite as Authors (Year) Title. American Mineralogist, in press.
DOI: https://doi.org/10.2138/am-2020-7189

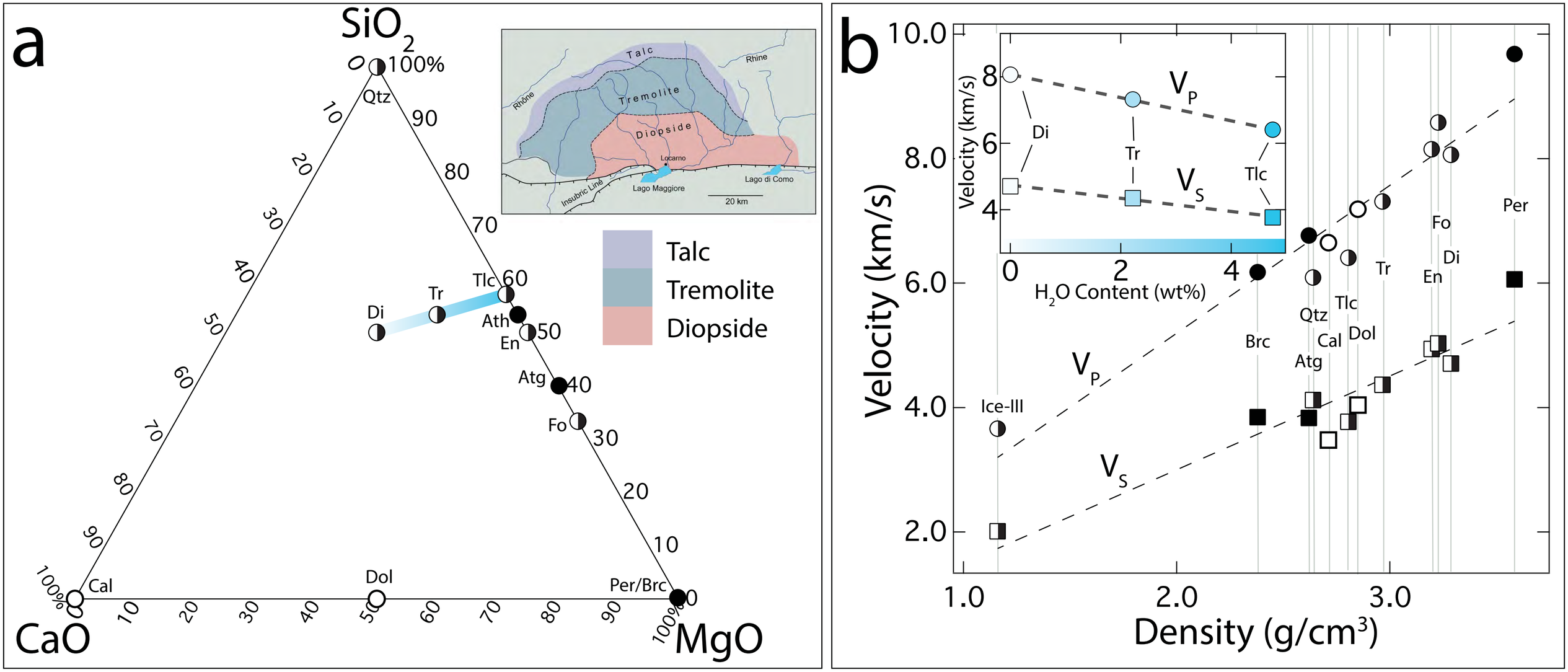

Figure 7

This is a preprint, the final version is subject to change, of the American Mineralogist (MSA)
Cite as Authors (Year) Title. American Mineralogist, in press.
DOI: https://doi.org/10.2138/am-2020-7189

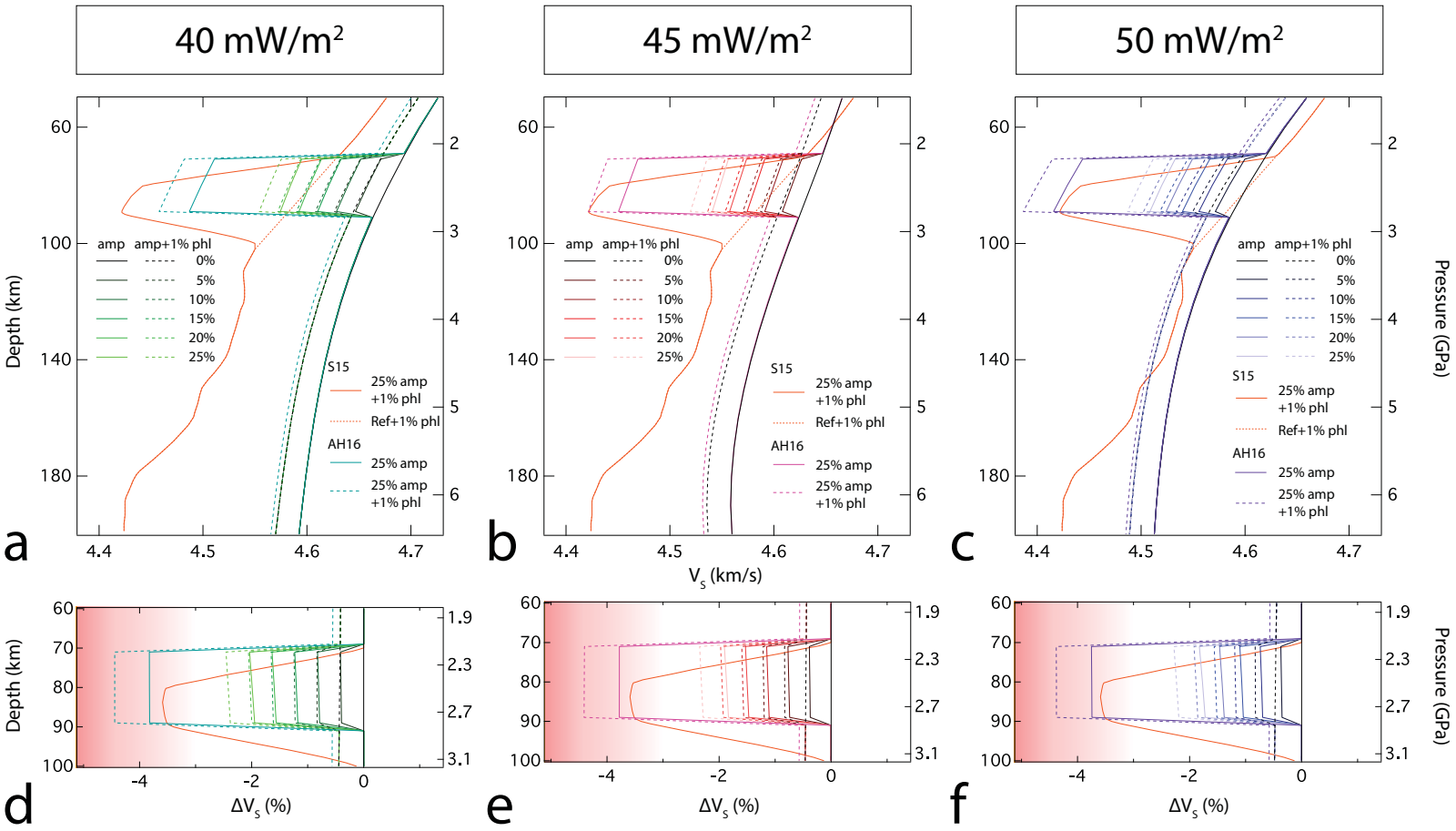

Figure 8